Department of Physics and Astronomy
Heidelberg University

Bachelor Thesis in Physics
submitted by

Johannes Hensler

born in Überlingen (Germany)

2023

Simulation of proton reaction cross-section measurements using ALPIDE monolithic active pixel sensors

This Bachelor Thesis has been carried out by Johannes Hensler at the
Physikalisches Institut, Heidelberg University (Germany)
under the supervision of
Prof. Dr. Silvia Masciocchi

Abstract

The reaction cross-section describes the probability of inelastic interactions when particles pass through a medium. This quantity is crucial in various scientific fields, including medical physics, aerospace, and high-energy physics.

The reaction cross-section can be measured via the attenuation method. In preparation of a future test beam, this thesis investigates a variant of this method using a particle telescope of Monolithic Active Pixel Sensors (MAPS) through a dedicated Geant4 simulation. The aim is to assess the feasibility of measuring the reaction cross-section of impinging protons ranging from 48 to 232 MeV using ALICE Pixel Detectors (ALPIDE).

The proposed measurement is presented and implemented in the simulation. Important measurement signatures are analysed and a virtual measurement explores the potential data correction using the models of the simulation.

The findings show that a measurement using MAPS is feasible and the simulation can effectively correct the raw data. Careful consideration is essential when selecting the target thickness, as it can significantly impact both the statistical uncertainty of the cross-section and the uncertainty of the reaction energy.

Zusammenfassung

Der Reaktions-Wirkungssquerschnitt beschreibt die Wahrscheinlichkeit von inelastischen Wechselwirkungen beim Durchgang von Teilchen durch ein Medium. Diese Größe ist in verschiedenen wissenschaftlichen Bereichen wie der medizinischen Physik, der Luft- und Raumfahrt und der Hochenergiephysik von entscheidender Bedeutung.

Der Reaktions-Wirkungssquerschnitt kann mit Hilfe der Dämpfungsmethode gemessen werden. In Vorbereitung eines zukünftigen Teststrahls wird in dieser Arbeit eine Variante dieser Methode unter Verwendung eines Teilchenteleskops mit Monolithic Active Pixel Sensors (MAPS) durch eine Geant4-Simulation untersucht. Ziel ist es, die Durchführbarkeit der Messung des Reaktions-Wirkungssquerschnitt von auftreffenden Protonen im Bereich von 48 bis 232 MeV mit ALICE Pixel Detektoren (ALPIDE) zu bewerten.

Die vorgeschlagene Messung wird vorgestellt und in der Simulation implementiert. Wichtige Messsignaturen werden analysiert und eine virtuelle Messung untersucht die mögliche Datenkorrektur unter Verwendung der Simulationsmodelle.

Die Ergebnisse zeigen, dass eine Messung mit MAPS möglich ist und die Simulation die Rohdaten effektiv korrigieren kann. Bei der Auswahl der Targetdicke ist eine sorgfältige Abwägung erforderlich, da sie sowohl die statistische Unsicherheit des Wirkungsquerschnitts als auch die Unsicherheit der Reaktionsenergie erheblich beeinflussen kann.

Contents

1. Interactions of particles with matter

The detection of particles relies on exploiting their interaction with matter. When a particle traverses matter it transfers energy, allowing for the deduction of particle properties by comprehending the details of these interactions. Generally, particles encounter multiple different interactions during their passage through matter, unless absorbed in the first interaction. Therefore, particle detectors specialise on various interactions to infer properties of the detected particles [30].

This chapter provides a brief introduction to the fundamental particles and forces forming the Standard Model of particle physics, as well as the most important interactions of particles with matter in the scope of this thesis.

1.1 The Standard Model of particle physics

The desire of particle physics is to understand what matter is made of. It wants to reveal the secrets of the composition of matter and the resulting phenomena that are observed. The most successful theory to explain the laws of nature, the Standard Model, expresses itself through two distinct, fundamental vocabularies. It uses elementary particles and the forces between them to formulate the surrounding world. The physics described by the Standard Model represents a unified picture since the forces between fundamental particles are themselves mediated by exchanges of particles [45].

The universe seems to be formed by only a few elementary particles, which can be seen in figure 1.1. They can be divided into two groups based on an intrinsic property, their spin.

The fermions, often referred to as the matter particles, are spin-half particles, whose dynamic is described by the Dirac equation of relativistic quantum mechanics [45].

The bosons, on the other hand, have an integer spin and mediate the forces of interaction between the fermions. In the Standard Model the matter particles are subject to three fundamental forces: the strong, electromagnetic and weak force. The fourth know fundamental force, gravity, is not included in the Standard Model. However, since the gravitational force is very small it can be neglected for particle interactions [45].

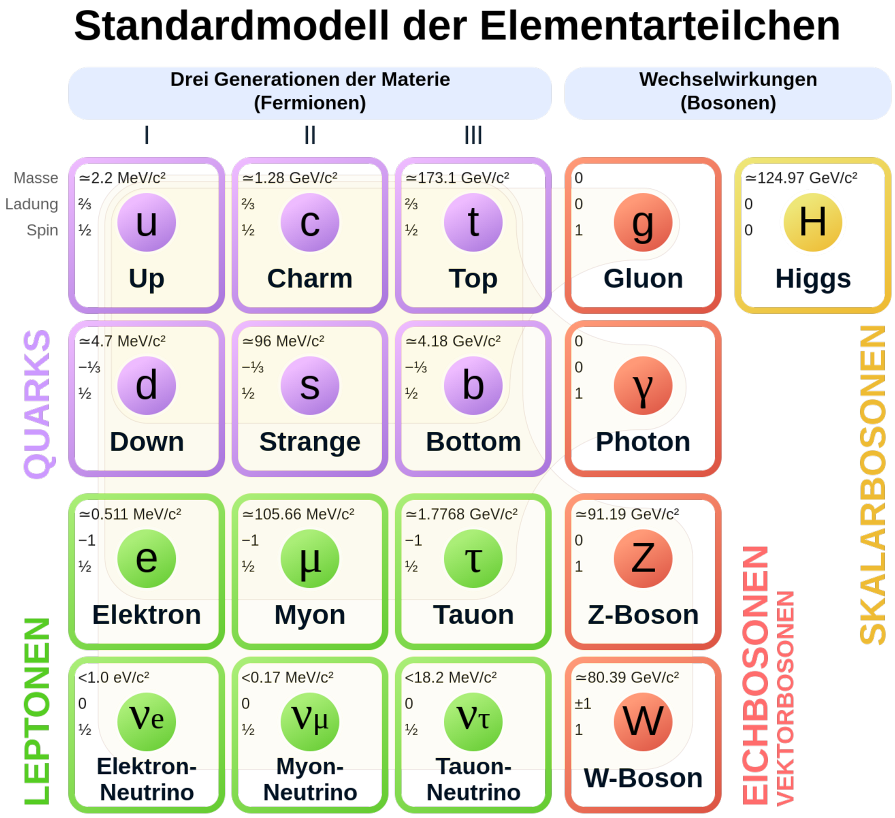

Figure 1.1: Schematic overview of the fundamental particles in the Standard Model [17].

The successful description of a wide range of experimental data by the Standard Model grants its significance for modern particle physics [45].

Fermions

The twelve fermions are subject to the fundamental forces and can be categorised by the forces they undergo. Quarks carry the charge of the strong interaction, the color charge, and are therefore affected by the strong force, whereas the leptons do not. Neutrinos are the only particles not experiencing electromagnetic interaction since they are electrically neutral. All twelve particles take part in weak interactions.

For each of the fundamental particles there exists a corresponding antiparticle with opposite charge but same mass, which is a consequence of the Dirac equation [45]. Due to the confinement nature of the strong interaction, quarks are never observed freely. They are confined in colourless bound states, called hadrons. Hadrons consisting of three quarks are referred to as baryons, whereas states of one quark and one anti-quark are called mesons.

Bosons

Classically, electromagnetic forces are described by scalar potentials. This formulation rises the question how momentum is transferred over distance without a mediating body being present [45].

Modern particle physics describes each force with a quantum field theory (QFT) corresponding to the exchange of a spin-1 force-carrying particle [45]. The photon is the exchange particle of the electromagnetic force in the theory of quantum electrodynamics (QED), the massive Z^0 and $W^{\pm}$ for the weak force and eight massless gluons carry the strong force in the theory of quantum chromodynamics (QCD).

The Higgs-Boson completes the Standard Model as it is currently known. The Higgs is, unlike all the other boson, a spin-0 scalar particle and plays a special role. It provides the mechanism to acquire the mass for all other particles [45].

1.2 Ionisation and excitation of charged particles

Charged particles traversing a medium interact electromagnetically with the electrons of the atoms. During these processes the incoming particle loses part of its kinetic energy through two distinct processes. The transferred energy can excite the electron into a higher state in the atom. However, it can also remove the electron completely from the atom, which is referred to as ionisation. Between the two, ionisation is of greater importance and the dominant process of energy loss [35].

The mean energy loss through ionisation is described by the Bethe-Bloch equation [30]:

$$-\left\langle \frac{\mathrm{d}E}{\mathrm{d}x} \right\rangle = 4\pi N_{\mathrm{A}} r_e^2 m_e c^2 \rho \frac{Z}{A} \frac{z^2}{\beta^2} \left[\frac{1}{2} \ln \frac{2 m_e c^2 \beta^2 \gamma^2 T_{\mathrm{max}}}{I^2} - \beta^2 - \frac{\delta(\beta\gamma)}{2} - \frac{C(\beta\gamma, I)}{Z} \right] \tag{1.1}$$

N_{A}	-	Avogadro number	Z, A	-	atomic and mass number of absorber
r_e	-	classical electron radius	T_{max}	-	max. energy transfer in one collision
m_e	-	electron mass	I	-	mean excitation energy
z	-	charge of incident particle	$\delta(\beta\gamma)$	-	density effect correction
β	-	ratio of v to c	$C(\beta\gamma, I)$	-	shell-correction
γ	-	Lorentz factor	ρ	-	density of absorber

The Bethe-Bloch formula expresses how particles are stopped in matter and is therefore also called stopping power [30]. The mean energy loss normalised to the density of the medium, also referred to as mass stopping power, is given by

$$-\frac{1}{\rho}\left\langle\frac{\mathrm{d}E}{\mathrm{d}x}\right\rangle \quad \text{with units of} \quad \frac{\mathrm{MeV\ cm}^2}{\mathrm{g}}. \tag{1.2}$$

This material density independent mean energy loss is shown in figure 1.2a.

The function features a characteristic minimum around $\beta\gamma = 3 - 4$. Particles in that regime are also referred to as minimum ionising particles since they lose a minimal amount of energy.

For low $\beta\gamma$, the particle loses more energy as the momentum transfer increases with the effective interaction time, which is longer for slower particles [30]. If the velocity of the particle is close to the electron orbital velocity the assumption that the electrons are at rest is no longer valid. Therefore, a so called shell correction is applied.

For large $\beta\gamma$ the transverse extension of the electric field increases due to Lorentz contraction, which leads to an increase of the energy loss. The increase for highly relativistic particles, however, is limited due to the polarisation of the medium. In that region, the electric field far from the particle path is effectively shielded, which reduces the energy loss due to the reduced long range contributions (density correction) [30].

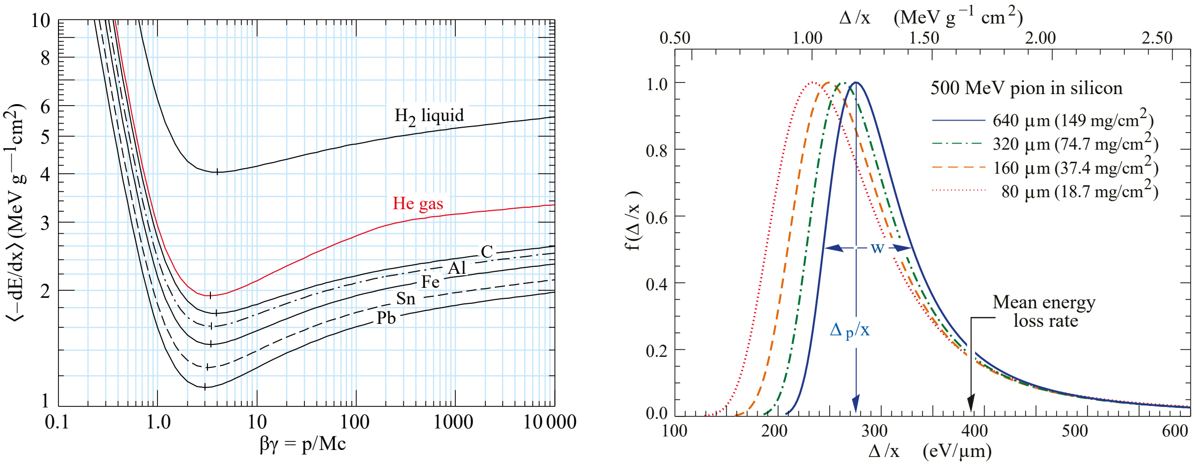

(a) (b)

Figure 1.2: Mean energy loss through ionisation as a function of $\beta\gamma$ normalised to the density and for different materials (a) [50]. Straggling functions for 500 MeV pions in silicon, normalised to unity at the most probable value Δ_p/x (b)[50].

The Bethe-Bloch formula describes the average energy loss. However, the energy loss process is of statistical nature, as the number of individual ionisation processes as well as the emitted energy can vary. This leads to fluctuations of the energy lost by a charged particle, also referred to as Landau fluctuations [30].

For thin materials, where only a small number of ionisation/excitation processes occur, the mean energy loss no longer accurately describes the actual energy loss due to fluctuations. In such cases, the Landau-Vavilov distribution can be used. The energy transfer fluctuations result in an asymmetric energy loss probability density function, denoted as $f(\Delta/x)$ or the energy straggling function (see figure 1.2b). Here, Δ describes the energy loss of a particle traversing a material with a thickness of x. This function comprises a Gaussian part from the numerous ionisation processes with small energy loss and a tail towards large energy loss values. The latter is caused by relatively rare, hard collisions where a substantial amount of energy is transferred to a single electron, often referred to as a δ-electron [30].

The maximum kinetic energy of δ-electrons can be calculated by considering the kinematics of an elastic collision [30]:

$$T_{\mathrm{max}} = \frac{2m_e c^2 \beta^2 \gamma^2}{1 + 2\gamma m_e/M + (m_e/M)^2} \approx 2m_e c^2 (\beta\gamma)^2 \qquad \text{for } \gamma m_e \ll M, \tag{1.3}$$

where M is the mass of the incident particle.

1.3 Elastic scattering

In elastic scattering the kinetic energy of the incident particle is conserved in the center-of-mass system but its trajectory is deflected. The kinetic energy of the particle is not conserved in the laboratory system, as opposed to the total kinetic energy of the colliding system.

Contrary to elastic scattering, in inelastic interactions, parts of the kinetic energy of the incident particle is lost to excite inner degrees of freedom, leading to a break in kinetic energy conservation. Inelastic interactions are also referred to as nuclear reactions. Depending on the energy of the incoming particle, different types of reactions can occur.

In one scenario, the incident particle can scatter inelastically, resulting in an outgoing particle that is identical to the incoming particle, but the target nucleus is left in an excited state. Alternatively, the reaction can be a so-called breakup reaction, where one or more particles are emitted from the target nucleus, and the incident particle is not necessarily present in the final state.

This section will cover the most important elastic interactions and the following section will cover the inelastic interactions.

1.3.1 Rutherford scattering

Charged particles are scattered in the Coulomb fields of nuclei, a process called Rutherford scattering. This interaction is mediated by the electromagnetic force. The scattering off a single nucleus is quantified by the Rutherford cross-section [30]

$$\frac{\mathrm{d}\sigma}{\mathrm{d}\Omega} = z^2 Z^2 \alpha^2 \hbar^2 \frac{1}{\beta^2 p^2} \frac{1}{4 \sin^4(\theta/2)}, \tag{1.4}$$

where θ is the scattering angle, α the dimensionless fine structure constant, $\hbar$ the reduced Planck constant and p the momentum of the incident particle. The differential cross-section can be understood as the number of particles scattered into an element of solid angle $\mathrm{d}\Omega$ per unit time, target particle and incident particle flux. A more comprehensive discussion of cross-sections and their importance will be given in chapter 3.

1.3.2 Nuclear scattering and Coulomb-nuclear interference

Elastic scattering is a process not only mediated by the electromagnetic force, but also by the strong force. The strong interactions are traditionally also referred to as nuclear or hadronic interactions [7].

In principle, these nuclear interactions should be described by QCD. However, experimental data reveals that their main contribution predominantly arises from the non-perturbative sector of QCD. Consequently, due to the absence of methods for a direct solution of these QCD equations, the theoretical knowledge of these strong interactions remains limited [19].

For this reason, experimental data studying the hadronic contribution holds special interest. The nuclear amplitude cannot be directly observed in the pure hadronic differential cross-section. However, both amplitudes contribute to an effect of Coulomb-nuclear interference in the differential cross-section. Consequently, with knowledge of the Coulomb amplitude, the interference provides access to information about the nuclear amplitude [7].

1.3.3 Multiple Coulomb scattering

Charged particles are deflected by many small-angle scatterings when traversing a medium. The major contribution is caused by Coulomb scattering as described by the Rutherford cross-section. For hadronic projectiles however, also the strong interactions contribute to the multiple scattering [50].

Many small-angle scatterings result in a net scattering and displacement distribution, which can be described by a Gaussian distribution, following the central limit theorem. However, these distributions also display non-Gaussian tails arising from less frequent hard scattering events. The Molière theory provides a suitable representation for these distributions.

In the small-angle Gaussian approximation the projected multiple scattering angular distribution is specified by the standard deviation θ_0 [50]:

$$\theta_0 = \theta^{\text{rms}}_{\text{plane}} = \frac{13.6\ \text{MeV}}{\beta c p}\ z \sqrt{\frac{x}{X_0}} \left[1 + 0.038 \ln\left(\frac{x z^2}{X_0 \beta^2}\right)\right]. \tag{1.5}$$

Here, x is the thickness and X_0 the radiation length of the scattering medium. The scattering into $\theta_{\text{plane,x}}$ and $\theta_{\text{plane,y}}$ are independent and identically distributed.

The standard deviation of the projected offset of incoming to outgoing trajectory $y^{\text{rms}}_{\text{plane}}$ is given by [50]:

$$y^{\text{rms}}_{\text{plane}} = \frac{1}{\sqrt{3}}\theta_0. \tag{1.6}$$

1.4 Inelastic interaction of hadrons with matter

In the interaction of hadrons with a nucleus, two possibilities arise. The first is elastic scattering, as described in the previous section. The second possibility is that the hadron will initiate a nuclear reaction, which will be discussed in what follows [11].

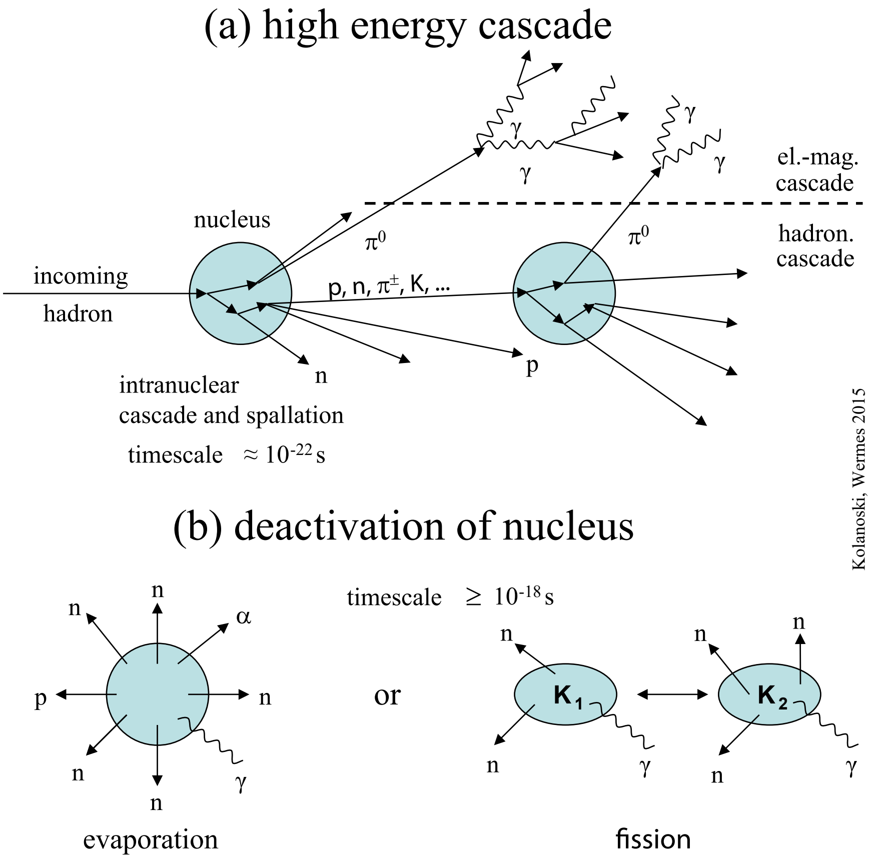

Figure 1.3: Schematic overview of the interaction of hadrons in matter. Development of a high energy cascade (a) and deactivation of nucleus (b) [30].

In a dense medium, the incoming hadron can undergo inelastic interactions with a nucleus, resulting in the production of highly energetic secondary particles predominantly in the forward direction. This initial interaction primarily occurs with a single nucleon of the nucleus, while the other nucleons are considered as spectators [30]. As a consequence of the inelastic reaction, the incident particle is removed from the primary beam of unaffected particles [32]. This can occur either through the destruction of the particle during the reaction or through inelastic scattering.

The produced secondary particles propagate through the nucleus and can also engage in inelastic interactions. A portion of the energy from the incoming particle and the secondary particles highly excites the nucleus, leading to a phase known as spallation. During this phase, energy is emitted through the emission of nucleons, light nucleus fragments, and photons. This process is also referred to as an intranuclear cascade, where the particles interact inside the nucleus until their energy decreases below the threshold for inelastic interaction, or they exit the nucleus [30]. The particles that left the nucleus can engage further in inelastic interactions with other nuclei in the material and possibly leave the material. The development of an intranuclear cascade is shown in figure 1.3.

After the spallation phase, the nucleus remains in a highly excited state and predominantly de-excites through evaporation, where nucleons and nucleus fragments are emitted. In some cases, fission is also possible [30].

2. ALICE at the LHC

The quest to expand the fundamental understanding of the matter in the universe and its underlying mechanisms drives the development of new experiments, aimed at either validating existing theories or uncovering new insights at the forefront of human knowledge.

One research facility dedicated to high-energy physics research is the European Council for Nuclear Research (abbreviated as CERN) near Geneva. CERN features a unique accelerator complex consisting of a succession of machines designed to accelerate particles to increasingly higher energies, culminating in the Large Hadron Collider (LHC), which currently holds the title of the largest particle accelerator with a circumference of 27 kilometers [27]. Guided by a strong magnetic field, created by superconducting electromagnets, particles travel at record energies of 6.5 TeV per beam and collide at four intersection points [26].

At each of these collision points, an experiment is conducted to study the outcome of the collisions. Alongside LHCb, ATLAS and CMS, the ALICE experiment is one of the main experiments at CERN and will be discussed in more detail below. The second part of this chapter bridges the gap between ALICE and reaction cross-sections by unravelling the significance of these cross-sections for the experiment and for various other application fields.

2.1 ALICE

ALICE (**A** **L**arge **I**on **C**ollider **E**xperiment) is a particle detector dedicated to studying heavy-ion physics at the LHC. Its design is optimised to address the physics of the Quark Gluon Plasma (QGP), a state of matter believed to have formed shortly after the Big Bang [3].

To study the properties of the QGP, it is reproduced in laboratory conditions through the collision of heavy nuclei (Pb-Pb). The physics program of ALICE is complemented with collisions of lighter ions (Xe-Xe, O-O), to vary energy density and interaction volume [42]. Data taking of proton-proton (pp) collisions is part of the program as well, to study small systems and search for thresholds of QGP formation [14].

The physics requirements of measuring sensitive signatures from QGP observables and the expected experimental conditions in heavy-ion collisions have driven the detector design. The resulting detector measures 16 m × 16 m × 26 m, weighing approximately 10000 tons [3]. The cylindrical shaped detector consists mainly of two parts (see figure 2.1): a central barrel and a forward muon spectrometer. The barrel covers a polar angle relative to the beam axis from 45° to 135° and is surrounded by a solenoid magnet to allow momentum measurements [3].

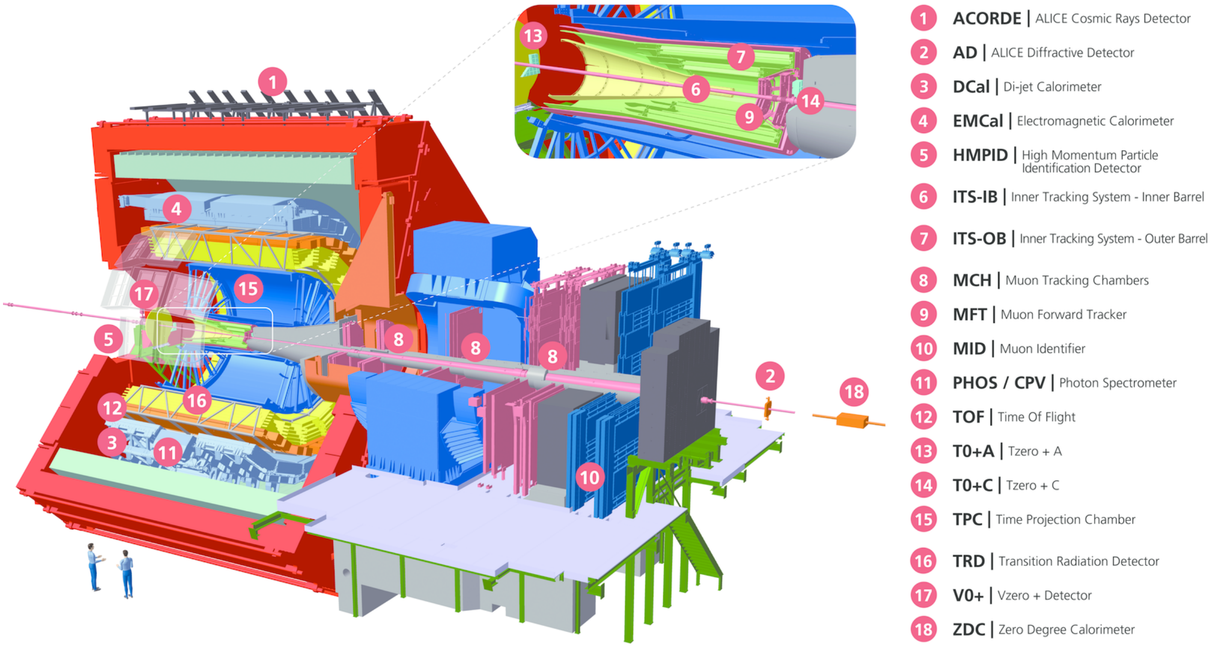

Figure 2.1: Schematic of the ALICE detector with labeled sub-detector systems [43].

To cope with the high multiplicity of particles in heavy-ion collisions mostly three-dimensional hit information is used to track the particle trajectories [3]. The innermost sub-detector of the central barrel is the recently upgraded **Inner Tracking System 2 (ITS2)**. Consisting of seven layers of silicon detectors it allows for reconstruction of the primary vertex, secondary vertices of heavy flavor particle decays and tracking of low-momentum particles.

Due to the high particle density close to the interaction point, a high granularity for the ITS2 is needed, which is achieved by the use of ALPIDE sensors, the flagship Monolithic Active Pixel Sensor (MAPS). The concentric ITS2 is structured into two parts. The Inner Barrel at 23 mm from the interaction point, containing the innermost three layers, and the Outer Barrel, which consists of the Middle and Outer Layers [41].

Through a closer placement of the detector to the interaction point, reduction of the material budget and higher granularity of the fully pixelated detector, not only the impact parameter resolution got improved, but also the tracking efficiency and transverse momentum resolution of low momentum particles [41].

Following the ITS2 in the concentric hierarchy of ALICE is the **Time Projection Chamber (TPC)**. The TPC is the heart of tracking and particle identification in the central barrel. Charged particles traversing the gas-filled volume will liberate electrons through ionisation, which drift along the uniform electric field towards the end caps, where position and arrival time is measured. Thus the trajectory of the particles can be reconstructed and by measuring the deposited energy the particle can also be identified.

Even further away from the interaction point lies the **Transition Radiation Detector (TRD)**. If a charged particle traverses a boundary between materials with different dielectric constants there is a probability that a photon is emitted. The intensity of the transition radiation depends linearly on the Lorentz factor and is typically very low (less than one detectable photon per crossing for $\gamma = 1000$) [30]. Due to the sensitivity for the Lorentz factor, electrons can be distinguished from other charged particles. In addition, the TRD enhances the resolution at high transverse momentum by increasing the measured track [3].

The **Time Of Flight (TOF)** detector measures the time a particle travels from the primary vertex and therefore gives information about the velocity of particles. Combined with a measurement of the momentum, the TOF contributes to the particle identification (PID) in the intermediate momentum range. The TOF, as it is also located in the central barrel, features a cylindrical symmetry and consists of Multigap Resistive Plate Chambers (MRPC) [25].

The particle identification system of ALICE is complemented by the **High Momentum Particle Identification Detector (HMPID)**, which is based on Ring Imaging Cherenkov counters (RICH). Charged particles that traverse the medium of the detector faster than the phase velocity of light in that medium emit Cherenkov radiation inside a cone, with a velocity-dependent angle.

The calorimeters of ALICE are furthest away from the interaction point. The **Electromagnetic Calorimeter (EMCal)** is a shashlik-type lead-scintillator sampling calorimeter used to determine highly energetic photons, electrons, neutral pions and jets of particles [23]. The EMCal is accompanied by the **PHOton Spectrometer (PHOS)**, which is primarily dedicated to measuring the direct, thermal radiated photons, to probe the initial state. The PHOS is realised by a homogeneous lead-tungstate calorimeter [24].

The above mentioned main components of the detector are complemented by a variety of smaller specialised systems. An overview is given in [3].

2.2 Motivations for investigating nuclear data

Besides the theoretical interest in nuclear reaction cross-sections, there is also a growing need for nuclear data in a variety of application fields [32].

Since the first treatment at Lawrence Berkeley Laboratory, protons have been used for over 50 years to cure deep-seated tumors and other medical conditions [40]. Proton therapy utilises the Bragg peak effect, where a charged particle passing through tissue gradually loses energy via ionisation, but the peak dose is deposited just before the particle comes to a stop. Consequently, the majority of the energy is concentrated in a confined area. This allows for precise targeting of tumors and sparing of healthy surrounding tissue.

However, a part of the protons will also undergo inelastic reactions inside the tissue. The produced secondary protons comprise up to 10 % of the total absorbed energy dose in a high-energy proton treatment, therefore they have a small but non-negligible impact on the spatial dose distribution [40].

Besides clinical concerns, there are also ones about personnel and equipment in connection with inelastic reactions. Certain beam production and delivery equipment is exposed to the proton beam, which leads to proton-induced neutron production [40]. Neutrons create potential safety risks to personnel and electronics. In conclusion, a deeper understanding of nuclear reactions may improve therapeutic methods and the safety of proton treatments.

High-energy cosmic radiation is composed mainly of protons, alpha particles, and heavier ions that originate both within and outside our galaxy. The primary cosmic particles interact in the atmosphere of the earth and produce secondary particles, including neutrons, which penetrate air- and spacecraft. Therefore the nuclear interaction of particles with biological matter is not only of interest in proton therapy but also in the aerospace industry concerning astronauts and passengers of commercial aircraft.

The hazards posed by galactic cosmic rays present significant obstacles to manned, long-term deep-space exploration missions. Assessing the risks associated with these missions requires the development of reliable heavy-ion transport codes [33].

It has been found that flashes in the human eye experienced by astronauts are caused by two complementary mechanisms. Direct ionisation and excitation in the retina, as well as proton-induced nuclear interactions in the eye that produce secondary particles. [12]. Therefore studying the interactions of particles with the elements found in natural tissue, air and shielding material is of interest.

Furthermore, cosmic radiation can influence or even permanently damage electronic devices. The energetic particle can change the state of a digital circuit by depositing energy in sensitive areas, which is known as a single event upset (SEU) [47]. This effect is not as strong at sea level due to the shielding of the atmosphere but increases with altitude. To gain knowledge on these effects the studying of interactions with silicon, but also the surrounding support materials is of special interest. Understanding inelastic nuclear interactions is essential in order to evaluate and mitigate the potential risks to both human health and electronic devices exposed to cosmic radiation.

The process of element synthesis and energy production in astrophysical objects is heavily influenced by the properties of nuclear reactions [28]. Accurate modeling of these environmental conditions requires not only information on energy release but also on the rates of relevant reactions. As a result, precise measurements of reaction cross-sections are crucial for improving astrophysical models.

In addition to medical and astrophysical applications, there is a significant need for nuclear data in high-energy physics. In the ALICE experiment, the reconstruction efficiency of (anti)(hyper) nuclei is crucial for determining the systematic uncertainty of derived quantities. This efficiency depends, among other factors, on the inelastic reaction cross-section in the detector materials. To account for this effect, the experiment uses a Geant4 simulation based on measurement data [43]. Therefore expanding and improving the measurements on reaction cross-sections possibly improves the systematic uncertainties in the reconstruction and as a consequence results in more precise measurements of the ALICE experiment.

Moreover, all data-driven simulation tools profit from precise measurements as it allows for extended quality reviews and overall improvement in the prediction.

The diverse range of applications of nuclear data requires information on various projectile and target nuclei, as well as different energy regions. Since it is impossible to cover this vast variety of combinations through measurements alone, a High-Priority Nuclear Data Request List (HPRL) was established to keep track of the most crucial nuclear data requirements. Among these requirements, the measurement of proton and neutron data is given high priority, as knowledge of the cross-sections of these two particles can significantly impact the uncertainties of predictions for other nuclides where no experimental data exists [44]. As many proton measurements for various nuclei exist nowadays, the goal of the possible measurement presented in this thesis could be to demonstrate the feasibility of such a measurement using MAPS and to potentially expand to unmeasured combinations of projectile nuclei in the future.

The choice of aluminium as the target nuclei for this study was based on its frequent use in the support structures of the ALICE detector. Additionally, it has a similar atomic number to silicon, which is commonly found in both electronic and detector components. In particular, this study is important for the proposed ALICE 3 experiment, which features a detector primarily composed of advanced silicon detectors [13].

The previous chapter emphasised the importance of obtaining nuclear data for a variety of applications, highlighting the significance of investigating proton-aluminium (p-Al) interactions. The main objective of this thesis is to develop a simulation to evaluate the feasibility of conducting a reaction cross-section measurement using MAPS. Furthermore, the simulation aims to support the planning process for such a measurement. By utilising this simulation, it becomes possible to analyse the impact of specific setup parameters, evaluate resulting background effects and gain insights into relevant physical interactions. This enables the identification and mitigation of potential sources of systematic and statistical uncertainties. In the case of protons, the simulation holds the potential to correct measured data, as a substantial amount of previously collected data and reliable models are available.

3. Introduction to reaction cross-section measurements

3.1 Interaction cross-sections

The cross-section σ is a measure for the quantum mechanical probability than an interaction occurs. It represents the fundamental physics in an interaction and depends on the kind and strength of the interaction. The cross-section can be interpreted as the effective cross sectional area associated with each target particle, that is seen by the incoming particle. Thus the cross-section marks the effective interaction area of each target particle and has the dimensions of an area [30, 45].

The probability of an interaction P is defined as

$$P = \frac{\dot{N}_{\mathrm{R}}}{\dot{N}_{\mathrm{in}}} = \frac{N_{\mathrm{R}}}{N_{\mathrm{in}}} \tag{3.1}$$

where $\dot{N}_{\mathrm{R}}$ is the interaction rate and $\dot{N}_{\mathrm{in}}$ the rate of incoming beam particles [30]. In many cases, including this thesis, both rates are constant in time. Therefore this ratio can also be expressed by the ratio of counts, as both are linearly dependent on the time.

The interaction probability P can also be thought of as the probability of a beam particle intersecting with the cross-section area of a target particle, given by

$$P = \frac{N_{\mathrm{T}}\ \sigma}{A_{\mathrm{T}}}, \tag{3.2}$$

with N_{T} as the number of target particles and A_{T} the target area exposed to the beam [30]. To generalise the number of exposed target particles N_{T}, the number of target particles per unit area n_{A} is introduced:

$$n_{\mathrm{A}} = \frac{\rho\ t\ N_{\mathrm{A}}}{M} \implies N_{\mathrm{T}} = n_{\mathrm{A}}\ A_{\mathrm{T}}. \tag{3.3}$$

Here, ρ is defined as the target mass density, M the molar mass of the target particles, t the thickness of the target material and N_A the Avogadro number. Using this definition equation 3.2 can be generalised to

$$P = \frac{n_\mathrm{A}\ A_\mathrm{T}\ \sigma}{A_\mathrm{T}} = n_\mathrm{A}\ \sigma. \tag{3.4}$$

By combining equation 3.1 and 3.4 an expression for the cross-section for a specific interaction can be deduced:

$$\sigma_\mathrm{R} = \frac{1}{n_\mathrm{A}} \frac{N_\mathrm{R}}{N_\mathrm{in}}. \tag{3.5}$$

3.2 Attenuation method

The reaction cross-section represents the probability that a particle undergoes an inelastic interaction while passing through matter. Over time, numerous different techniques to measure the total reaction cross-section were developed. Earlier on, triggered cloud chamber techniques where used to measure reactions of particles. For low energy protons the reaction cross-section was also determined by summing the partial cross-sections for all possible reactions [11]. The most efficient method is considered to be the attenuation method, where the attenuation of a particle beam in a target is examined. This technique encompasses various variants that are based on the same fundamental principle.

It is expected that inelastic interactions remove the projectile particles from the beam of unaffected particles. Thus, the intensity of the outgoing beam is attenuated with respect to the incoming beam. The attenuation of a beam of particles passing through matter is given by

$$N_\mathrm{out} = N_\mathrm{in} \exp\left(-n_\mathrm{A}\sigma_\mathrm{R}\right), \tag{3.6}$$

where N_out and N_in are the intensities of the attenuated beam and incident beam, respectively [11]. Here, σ_R represents the reaction cross-section. In reality, not only inelastic interactions contribute to the attenuation, but also a variety of other effects. Therefore, technically, this cross-section represents all effects that contribute to the attenuation. For this reason, the initial measurement needs to be corrected in order to extract the reaction cross-section.

For small values of $n_A\sigma_R$ compared to unity, equation 3.6 can be written (using Taylor series expansion) as

$$N_\mathrm{out} = N_\mathrm{in}(1 - n_\mathrm{A}\sigma_\mathrm{R}). \tag{3.7}$$

Therefore the cross-section can be measured by counting incoming and outgoing particles:

$$\sigma_\mathrm{R} = \frac{1}{n_\mathrm{A}} \frac{N_\mathrm{in} - N_\mathrm{out}}{N_\mathrm{in}} = \frac{1}{n_\mathrm{A}} \frac{N_\mathrm{reac}}{N_\mathrm{in}}, \tag{3.8}$$

where N_{reac} is the number of reaction events. This result shows that by examining the attenuation of a particle beam, the reaction cross-section can be obtained.

The method of measuring the attenuation can vary. The method that was found most efficient in the past is to count the number of reaction events directly by measuring the energy deposited after the target [11]. In this thesis a different method is investigated and will be discussed in the following section.

3.3 Proposed measurement using ALPIDE sensors

The proposed measurement is based on the attenuation method. It aims at quantifying the attenuation by measuring the intensity of the beam before and after the target. This approach has the initial disadvantage of limited accuracy, as the difference of two large numbers with almost equal value is used to determine the cross-section [11]. However, the approach has the potential to exploit the excellent tracking capability of the measurement setup to increase the rate of data taking by increasing the multiplicity of projectile particles in each event.

The method heavily relies on precise counting of incoming and outgoing particles. Therefore, a reliable measurement in front and behind the target is needed, which is accomplished through the usage of silicon pixel detectors in a construction called a particle telescope. It consists of multiple detectors, placed one after another in the beam path. If a charged particle passes one of these sensors, it creates electron-hole pairs along its flight path. These charge carriers diffuse through the sensor and are eventually collected by an applied internal electric field. ALPIDE (ALice PIxel Detector) chips, currently in use in the ITS2 of ALICE, are chosen for the tracking planes. They are Monolithic Active Pixel Sensors (MAPS) produced in the 180 nm CMOS imaging process of Tower Partners Semiconductor Co., Ltd.(TPSCo)[46]. A picture of the sensor is shown in figure 3.1. The ALPIDE sensors boast excellent position resolution of 5 µm, high detection efficiency of above 99 % and low material budget (sensors are thinned down to 50 µm) [2].

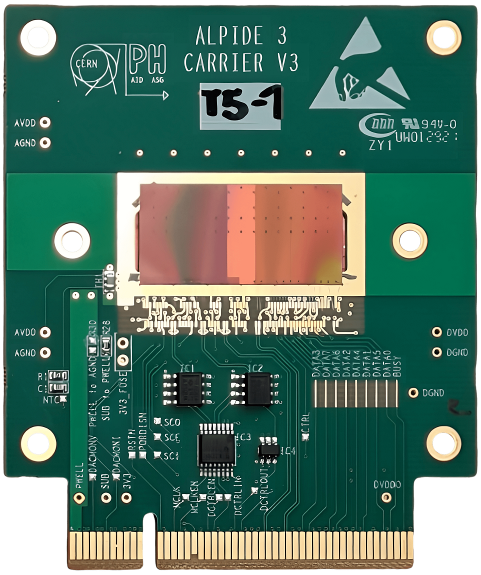

Figure 3.1: Single ALPIDE sensor on a carrier board.

Upstream of the target, three ALPIDE planes are used to track incoming particles.

Three tracking planes are selected because if only two tracking planes were chosen, the fit using a straight line or general broken line would have zero degrees of freedom [29]. As a result, the fit would become meaningless since the parameters cannot vary in this case. Therefore, a minimum of three planes is necessary to ensure that the particle can be accurately tracked in the actual experiment.

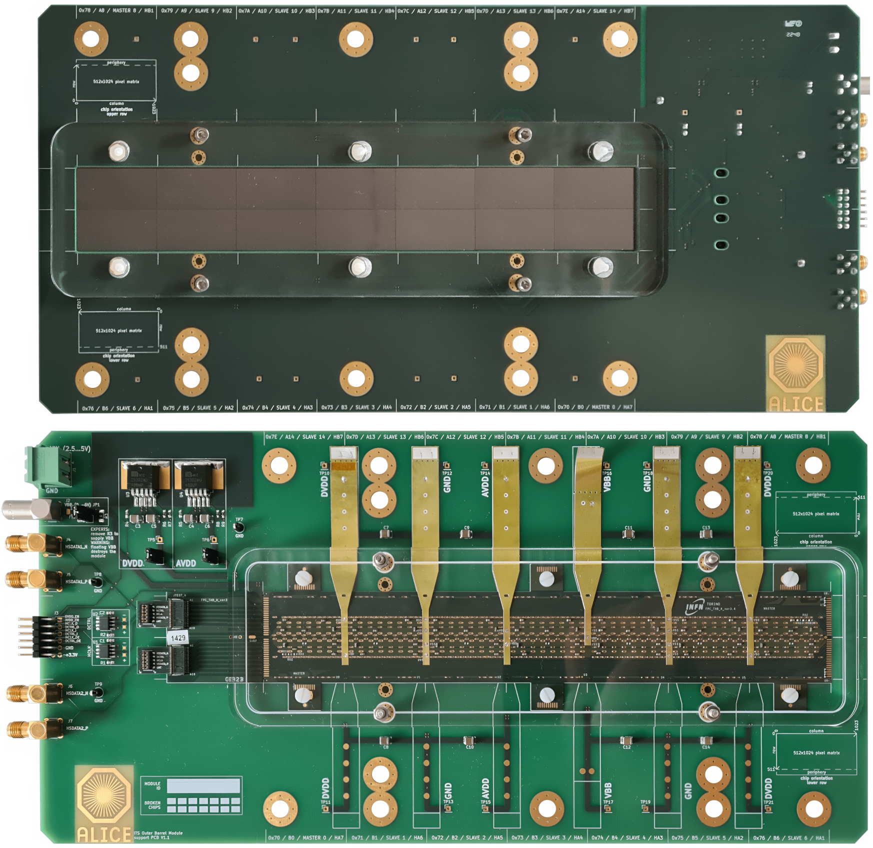

Figure 3.2: Outer Barrel Module (OBM) on a carrier board modified for educational activities. The sensor side is shown in the upper picture, while the lower picture shows the backside. An acrylic cover protects the sensors and fragile electronics during transport.

The setup for measuring the outgoing tracks differs slightly. Due to various interactions affecting the incoming projectiles within the target, the particles get deflected, some at angles that fall outside the acceptance of a similar three ALPIDE plane geometry. To minimise the number of unmeasured scattered particles after the target, it is necessary to maximise the acceptance window, which refers to the solid angle in which particles are detected. Therefore, two Outer Barrel Modules (OBM) are employed, in addition to three ALPIDE planes. As the name suggests, these modules are building blocks of the Outer Barrel in the ITS2 and consist of 14 ALPIDE detectors separated in two rows of seven detectors (see figure 3.2). By incorporating these additional layers, the acceptance in the y dimension experiences a slight increase, while the increase in the x dimension is substantial.

On the OBM the individual sensors are separated by small gaps. These gaps introduce the potential of missing particles that are very well centred. Using, for instance, one ALPIDE and the two OBM behind the target would significantly increase the acceptance, but a lot of particles would only create a hit on the ALPIDE and pass through the two OBM undetected. A slight intentional misalignment could potentially help mitigating this problem. However, to ensure reliability, the three ALPIDE sensors were chosen to cover the crucial central region. The operation of the individual ALPIDE sensors is well understood and there is plenty of experience with their use. In contrast, the knowledge and experience with the OBM on the modified carrier board in testbeam use are currently limited. Hence, the decision to employ three ALPIDE sensors also provides a contingency plan, ensuring the measurement can proceed even if the OBM were to fail. This redundancy in the setup enhances the overall reliability of the experiment.

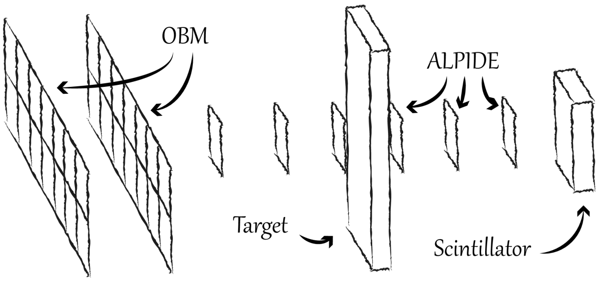

Figure 3.3: Conceptual sketch of the measurement setup.

A trigger signal is needed for data acquisition. For this purpose, a plastic scintillator is employed and placed in front of the setup. Particles can scatter in the scintillator or in the ALPIDE sensors before reaching the target, thus creating a trigger signal but no incoming track. Therefore, the idea of using a second scintillator in coincidence might seem appealing. However, it was decided against this approach as it would introduce additional material into the beam.

The arguments presented above provide insights into the factors considered when planning this measurement setup. It is important to note that this setup was chosen as a starting point. Further investigations may reveal that a different configuration is favourable to enhance the quality of the measurement.

A possible facility to conduct this experiment is the Marburg Ion Therapy Center, which can deliver protons in the kinetic energy range of 48-221 MeV.

4. Geant4

Geant4 (**Ge**ometry **an**d **T**racking) is a software framework that allows to perform simulations of the passage of particles through matter. It is based on modern C++ and uses Monte-Carlo methods. Geant4 finds its application in a vast variety of areas in science, from high-energy and accelerator physics to space engineering and medical science [5].

Simulations are helpful in high-energy physics in two distinct ways: They provide an important reference during the R&D phase of new detector technologies and they contribute to a better understanding of the response of installed detectors for physics studies. In order to create a virtual environment for the simulation, Geant4 handles the creation of specific geometries, tracking of particles, detector response, run-management, visualisation and user interface [8].

In this chapter, the basic concepts as well as the program flow of a simulation are explained to provide an understanding of the structure and behaviour of Geant4. Within this thesis, the framework will be used to simulate the passage of particles through an aluminium target in order to gain knowledge about important effects in the reaction cross-section measurement.

4.1 The structure of a simulation

To get insights on the functionality of Geant4, the vocabulary in which it is formulated needs to be understood. Due to the underlying object-oriented programming language, Geant4 is modular, where each module is represented in a C++ class. For this reason, this section will give a brief introduction to the most important classes in Geant4.

4.1.1 Geometry

The geometry system of Geant4 allows for the creation of complex detector geometries, including customised shapes and materials. This is essential for simulating realistic experimental setups and accurately modelling particle interactions in detectors. The demand of detector geometries is manifold, ranging from arrangements of a few simple shapes to hundreds of thousands of volumes for simulations of entire LHC experiments, such as the

ALICE detector system [4]. Defining geometries is realised in three distinct steps and can be seen in figure 4.1:

At first, a conceptual layer `G4Solid` is used to represent the pure three-dimensional spatial shape of a detector. These solids can consist of simple shapes, like boxes, trapezoids and spherical and cylindrical sections. Solids can also be combined by boolean operations such as union, intersection and subtraction, to create new shapes and therefore more complex geometries [5].

Solid volumes are combined with materials to create `G4LogicalVolume` objects. Thus logical volumes contain the shape and dimensions as well as all material-related properties and they can be thought of as the abstract representation of complete detector parts [15].

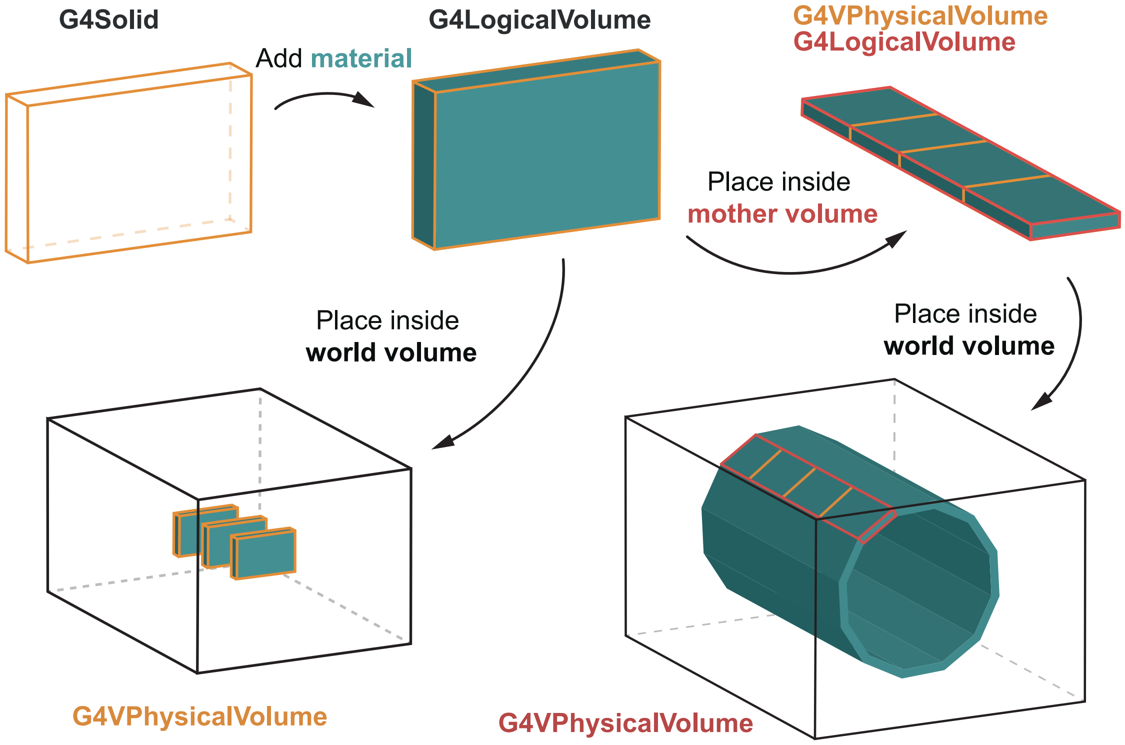

Figure 4.1: Schematic workflow of the geometry creation in Geant4. At first solid representations of the basic shapes are created. Materials are added to create logical volumes. The logical volumes serve as building blocks and they can be either directly placed within the world volume by creating a physical volume of the logical volume and specifying its location and rotation in the world space, or they can be nested inside another logical volume to construct modules that are then placed inside the world volume.

Logical volumes are building blocks that are used to construct bigger detectors or experimental setups. To handle the spatial positioning of these building blocks and their logical relations, `G4VPhysicalVolume` is introduced, which takes a logical volume and adds a spatial location and rotation, therefore placing it inside a mother volume [15]. The mother volume can be the world volume, which is the largest volume and contains all other volumes. Alternatively, it can be another logical volume, which therefore allows the creation of more complex building blocks (i.e. detector modules). The world volume is also used to describe the environmental conditions of the detector, such as the surrounding air.

4.1.2 Track and tracking

This category provides class objects related to the propagation of particles. An overview of the relevant tracking objects can be found in figure 4.2.

The particle transport in Geant4 is not continuous. The simulation is performed step by step, where each step is represented by a `G4Step` class [5]. Steps store a pre-step and post-step point as well as transient information (e.g. energy loss during this step, time passed). The length of each step depends on the applied physics models or limiting geometric boundaries and is described in more detail in section 4.2.

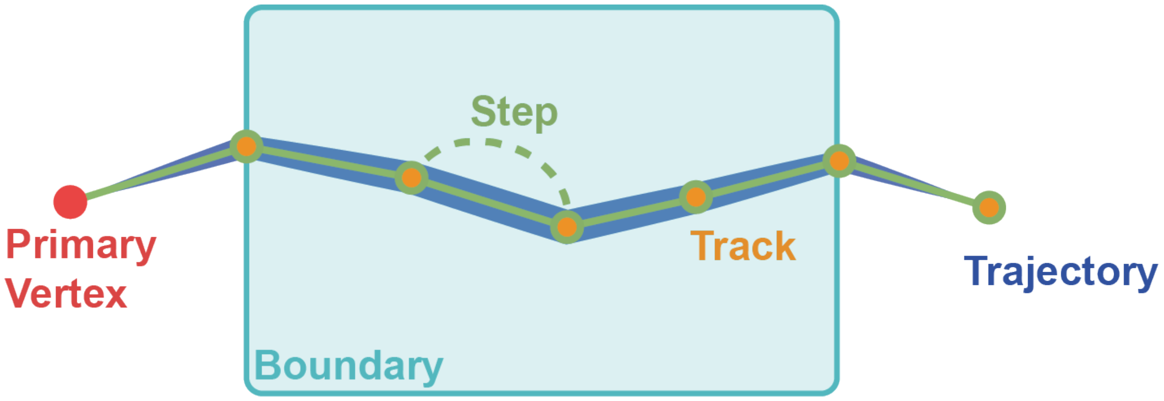

Figure 4.2: Schematic of tracking objects in Geant4. The particle, generated at the primary vertex, is propagated in steps, each with a pre- and post-step point as well as track information stored after each step. The trajectory sums up relevant information on the whole spatial trajectory at the end of each event. Adapted from [49].

A track is considered to be a snapshot of a particle, as it represents the instantaneous state of the particle after a step is completed. Therefore, it contains information about the current state of the particle such as energy, momentum and polarisation as well as static properties (e.g. type, mass and charge). It does not record information of previous steps, thus a track cannot be thought of a collection of steps [8, 15].

Since both track and step objects do not have a memory of previous steps and are not accessible at the end of an event, trajectories are implemented. A `G4Trajectory` stores specific information of tracks and steps to allow studies on the whole spatial trajectory at the end of an event [15].

4.1.3 Particle definition

Geant4 treats particles in a classical way, as point-like objects with well-defined momentum [49]. All particles are defined by a `G4ParticleDefinition` class which aggregates static information on the particle such as mass, charge, lifetime and a decay table [15, 49]. A list of particles is provided by the Physical Data Group encoding scheme (PDGID), which are created with their properties as listed in the PDG [1, 15].

4.1.4 Physics

The quality of a simulation is limited by its representation of the relevant physical interactions involved. Hence, it is important to know the limitations of a simulation to gain valuable knowledge.

Each physical interaction gets represented in simulation by a physics process class that describes how and when a specific physical interaction takes place [15]. For instance, the photoelectric effect is represented by the `G4PhotoElectricEffect` class, which handles the threshold energy and probability of the interaction as well as the production of a secondary electron. Henceforth, the term "process" refers to the description of a specific physical interaction in simulation.

A key feature of Geant4 is the generalisation and abstraction of interactions. Each process, independent of the underlying interaction, is treated the same way in terms of tracking. This is manifested in the underlying base class `G4VProcess`. It allows the user to create a process and assign it to a particle type and therefore creates a more customisable toolkit [15].

Each process includes two main methods, `GetPhysicalInteractionLength` and `DoIt`. The first one gives the step length from one space-time point to the next one. This is done by calculating the probability of this process based on the cross-section information of the underlying interaction (see section 4.2) [15]. In general, depending on the implementation of a process, these values are derived from either data, theory or empirical models.

The `DoIt` method is invoked to perform the interaction, meaning that at this point the energy, momentum, direction and position of the particle is changed, and secondary particles are produced [15]. To accommodate different types of interaction there are three implementations of `DoIt`. Firstly for continuous processes (i.e. ionisation, Cherenkov radiation), where the process is applied once for each step and accounts for all changes during the step accumulatively. Secondly, for processes at rest (i.e. decay at rest) where the process is applied only when the particle is at rest. And lastly discrete processes (i.e. secondary particle production by decay or interaction) which are performed at the end of a step [8].

However, the application developer does not need to create all processes of interest from scratch. There are many predefined processes the user can choose from.

Since in most of the cases not only one process is required, a collection of physics processes to be considered in the simulation is defined (physics list). The user can choose between creating a custom physics list or using an existing list provided by the toolkit [15].

4.1.5 Run and event

Classes of the run and event category are related to the generation of events and production of secondary particles. Their general role is to provide particles to be tracked [15]. A primary particle of specific type, momentum and direction is produced by using an implementation of `G4VPrimaryGenerator`.

One event contains the processing of a defined number of primary particles. These initial particles are pushed into a stack and processed one after the other until the stack is empty. At that point, the event contains information about the primary particles, vertices and the trajectories [8]. An event is realised in the `G4Event` class. The workflow of the program can be accessed before and after each event with the `EventAction` class to store event-specific quantities.

A run is defined as a collection of events with the same detector conditions, since the user cannot change either geometry or physics processes within one run [8]. It is realised in the `G4Run` class and allows for structural data taking. As for events, there is a `RunAction` class, that allows access before and after each run. This is usually used to store data for each run accordingly.

4.1.6 Hits

Stand-alone particle creation, propagation and interaction does not allow studying detector responses, therefore the missing key element needs to construct a bridge between geometry and tracking.

To realise sensitivity for a geometry, the logical volume is linked to a `G4VSensitiveDetector` class. This class handles the construction of hit objects using the information of the individual steps. To achieve this task, the `ProcessHits` method is invoked every time a step occurs inside the logical volume which is linked to the sensitive detector. It receives a `G4Step` object and allows the user to implement its own definition of a hit and the associated information stored in each hit [15].

4.2 Capturing physics processes

When a particle is travelling through matter, it is affected by a multitude of interactions. In simulation, this is reflected by various processes competing to be invoked. This can be particularly challenging to describe correctly in simulation, within an actual detector, where the particle typically passes through numerous volumes with distinct materials and shapes before eventually getting absorbed or decaying [5].

This chapter aims at a basic understanding on how the propagation and the interactions of a particle are simulated. In the first section the connection between the step length in simulation and the physical mean free path is explained. Afterwards, the concrete processing of a single step for one particle is discussed, which is extended to a whole event of one particle later on.

4.2.1 Step length and interaction point

The stepping mechanism is the core engine of the Geant4 tracking system. It is realised by the `G4SteppingManager` which handles the communication between all class objects relevant for tracking [15]. For an accurate simulation of the behaviour of a particle in a given system, it is necessary to consider the mean length before an interaction occurs for each relevant process in order to determine the appropriate time to activate it. To determine which process should be activated, the stepping needs to take these different mean free paths into account and to choose the step lengths such that it limits the step in an efficient and unbiased way [5].

Given a certain process, to compute the mean free path of a particle in a medium, the cross-section and the density of atoms in the detector are taken into account. For a pure material the volume density of atoms n is given by:

$$n = \frac{N_{\mathrm{A}}\rho}{A}, \tag{4.1}$$

where N_{A} is the Avogadro number, ρ the density of the material and A its molar mass [16]. This can be generalised for a compound material with:

$$n_i = \frac{N_{\mathrm{A}}\rho\, w_i}{A_i}, \tag{4.2}$$

where w_i is the mass fraction of the i^{th} material element and A_i the molar mass of the corresponding element [16].

The mean free path λ (interaction length) of an interaction is determined considering the total cross-section:

$$\lambda(E) = \left(\sum_i [n_i \cdot \sigma(Z_i, E)] \right)^{-1}, \tag{4.3}$$

where $\sigma(Z, E)$ is the total cross-section per atom of the process, which is dependent on the energy E of the incident particle and the atomic number Z of the target nucleus. The summation takes all elements of the compound material into account [16].

In the case of a particle decay, the mean free path is given by:

$$\lambda = \gamma \, v \, \tau, \tag{4.4}$$

where γ is the Lorentz factor, v the velocity and τ the mean lifetime of the particle [5].

Since the mean free path depends on the medium and projectile energy, it cannot be used directly to obtain the probability of interaction [16]. To calculate the distance to the interaction point or decay, the probability of passing a distance l without interaction is considered. It is derived as:

$$P(l) = e^{-n_\lambda}, \text{where } n_\lambda = \int_0^l \frac{dx}{\lambda(x)} \tag{4.5}$$

n_λ is the number of mean free path lengths travelled in l [5]. Note that this probability distribution is independent of material and particle energy. At the production of a particle, n_λ is sampled in a material-independent and unbiased way for each process by

$$n_\lambda = -\ln(\eta), \tag{4.6}$$

where η is a random number in the range of (0,1) [16].
The proposed step length for a process is then determined by:

$$s(x) = n_\lambda \cdot \lambda(x). \tag{4.7}$$

This is used to define the distance to the next interaction point and is updated after each step accordingly [16].

4.2.2 Processing of steps

Only through the abstraction of physics processes and therefore through the use of the same interface for each interaction it is possible to formulate one tracking algorithm, which is independent of the particle type and process [15].

One step of a particle is processed as illustrated in figure 4.3. If the particle is at rest, all active at-rest processes propose a step length based on the interaction they describe.

The process with the smallest step length will be invoked.

Is the particle not at rest, each discrete and continuous process proposes a step length based on the interaction it describes. Continuous processes also propose a step length since they might limit the step to preserve precision [5]. The smallest step length defines the next physical step length [16]. To ensure that the particle does not cross two media, the distance to the next volume boundary is calculated. The shorter length is chosen as the next true step length [15].

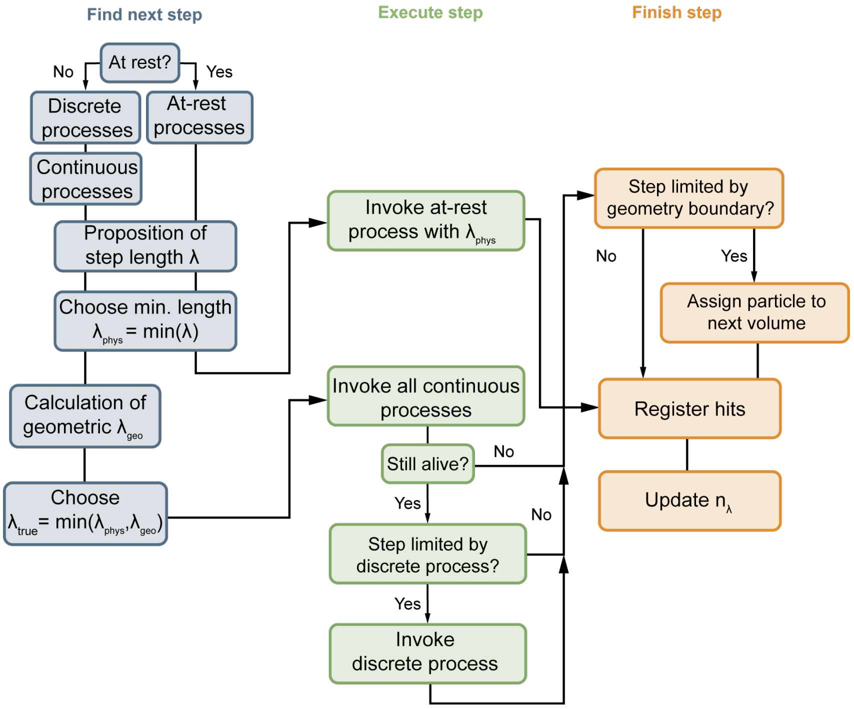

Figure 4.3: Simplified schematic diagram for processing one step

After the initialisation of the step, all active continuous processes are invoked to account for any changes of the particle properties during the step, such as energy loss. This activation of all continuous processes is independent of the limiting process that was determined by the proposed step-length. For instance if a specific decay (discrete process) had the smallest step length, the particle will still loose energy up until the particle decays at the end of the step. Same applies if the step is limited due to a geometric boundary. After all continuous processes are finished the track properties are updated and secondary particles are stored [15].

At this point, the kinetic energy of the particle is checked to see if it was absorbed during the step. If the particle still exists and a discrete process limited the step, it is now invoked, the track changes are updated and secondary particles saved once more [15].

If the step was restricted due to a geometric boundary, the associated volume the particle exists in is changed to the next medium. Therefore the post-step point is always hosted by the next medium for this case.

At this point the step object gets passed to the sensitive detector (if it exists) and the user can extract hit information [15].

In the end the number of mean free paths the particle propagates until it interacts is updated for each process that did not occur. This is done with

$$n'_\lambda = n_\lambda - \frac{\Delta x}{\lambda(x)}, \tag{4.8}$$

where Δx is the step length of the currently processed step. Hence the proposed step length of all processes, that are not activated, decreases until they have the smallest step length and trigger the step [16].

4.3 Program flow

Since the particle will most likely not propagate along its whole trajectory in one step, the next logical step is to extend the tracking of one step to multiple steps and take produced secondary particles into account. In the following, the flow of the program as a whole is explained by looking at the interplay of the main class objects.

4.3.1 Processing of events

To process events, a stack is used. The track objects of the primary particles are pushed into the stack during their generation. A schematic diagram of the event processing can be found in figure 4.4.

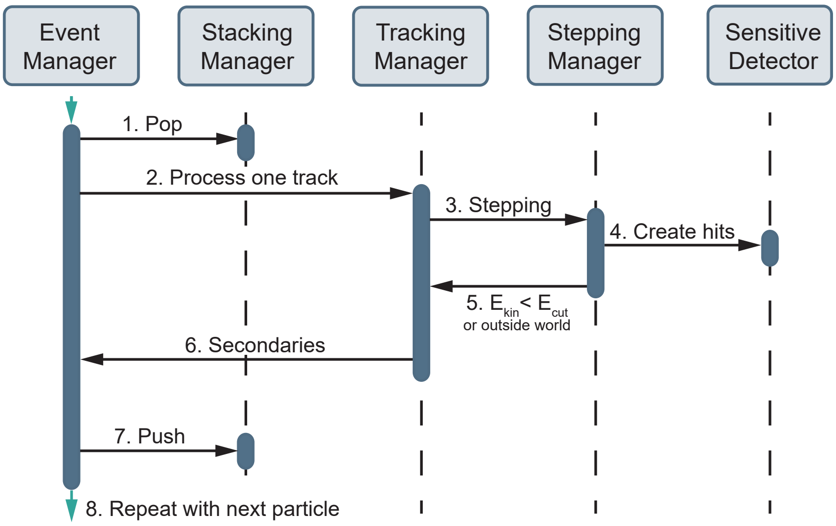

Figure 4.4: Schematic diagram for processing one event. Adapted from [8].

At the beginning of an event, the event manager pops out the first primary particle from the stack and passes it to the tracking manager, which will start the stepping manager to process the steps for this particle as described in section 4.2.2. During the step, secondary produced particles are saved to be pushed into the stack [8].

After each individual step it is checked whether the particle is still present inside the world volume and should be tracked. This is achieved by comparing the kinetic energy with a cut value, that can be defined by the user. If the processing of the particle is not finished, the next step will be taken until one criterion that ends tracking is reached [49].

If the stepping is finished with one particle, it pops out the next particle in the stack, until the stack is empty, and the event is considered finished.

4.3.2 Initialisation and run

A simulation consists of two phases, the initialisation and the run of the program (see figure 4.5 and 4.6 respectively).

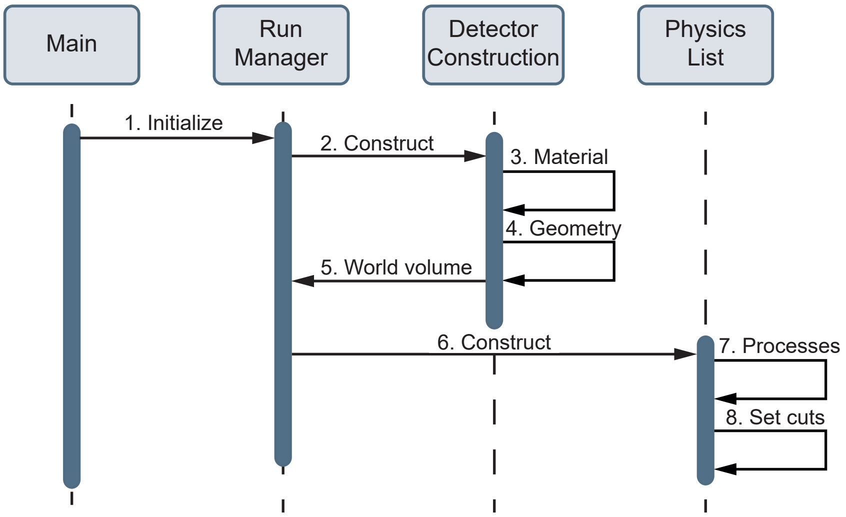

Figure 4.5: Schematic diagram of the initialisation phase. Adapted from [8].

As a first action, the user-created main program, which is the heart of the program, creates an instance of a `G4RunManager`. This class controls the whole flow of the program and manages the individual event loops in a run. Its task during the initialisation phase is to gather all information needed to build and execute the simulation, such as the detector construction, physics processes and primary particles [15]. The run manager constructs the provided geometry and materials as well as the defined physics lists and cuts. After the initialisation, the program is ready to receive primary particles to process.

In the run phase, the program breaks down tasks into smaller units for processing. It receives a run, the largest unit of a simulation, by the `BeamOn`-method. For each event the run manager initiates the closing of the geometry to prevent any changes of it during processing one event and allows for optimisation [15].

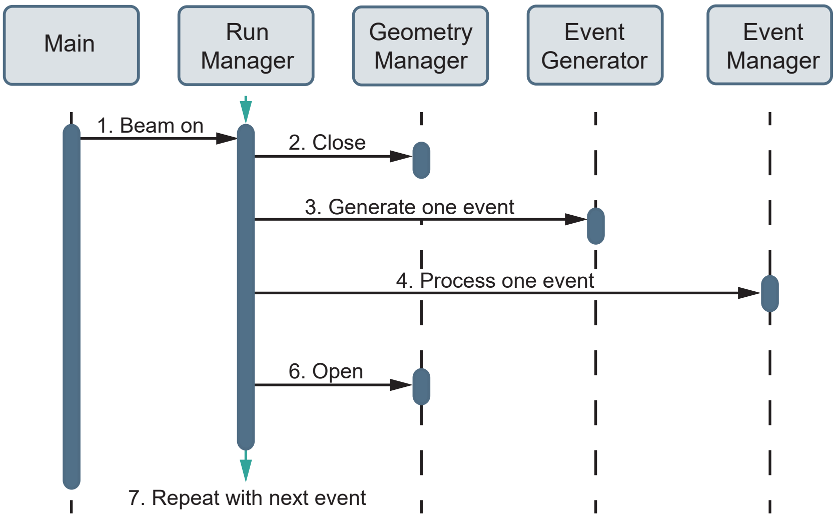

Figure 4.6: Schematic diagram of the run phase. Adapted from [8].

Afterwards an event is generated through the `G4EventGenerator` and processed as described in section 4.3.1 by the `G4EventManager`. When the event processing is finished, the geometry is opened again and the event-loop will restart.

5. Simulation of the reaction cross-section measurement

The proposed measurement will be investigated through simulation using the capabilities of Geant4, as described previously. The structure of the simulation, including the geometry, physics model and particle beam implementation will be presented. An overview of the sensitivity of the detector system will be provided, with specific details covered in subsequent sections. Following this initial overview section, it will be demonstrated that the simulation is capable of reproducing previously measured reaction cross-section data in the relevant energy regime. To gain insights into the fundamental factors impacting this measurement, an examination of the expected measurement signatures and their origins is conducted to identify contaminations present in the experiment. Subsequently, the influence of target thickness and edge effects is discussed. Finally, a virtual measurement is carried out to verify the assumptions made and conclusions from previous sections and show that a correction using the simulation is possible for the proton reaction cross-section.

5.1 Preliminary remarks

In order to understand the construction of the simulation and the established workflow, a few remarks need to be made. The aim of this simulation is to provide insights into the general attenuation measurement technique using a specific setup. The focus is on the particle interactions and resulting effects for the measurement and not on detector-specific technicalities and analysis-related challenges. Therefore, a few assumptions are made to keep the complexity and development time of the simulation limited.

In the simulation, a detection efficiency of 100 % for all charged particles is assumed which is appropriate since the ALPIDE efficiency was found to be above 99 % [41]. The simulation does not perform any kind of tracking for the particles in the detector telescope. Hits on the detectors are registered and assigned to a particle by the unique track id in the simulation. Hence, it is assumed that in the real experiment, each particle trajectory can be accurately reconstructed, achieving a tracking efficiency of 100 %. A detailed definition of tracks in the scope of this work will be given in section 5.4.

5.2 Structure of the simulation

The structure of the simulation will be explained successively, starting from an empty world volume with no functionality up to the whole sensitive setup with applied physical processes. The different classes, which were introduced in chapter 4, are used to define the geometry of the measurement setup, its functionalities and the physics processes that are considered in the simulation.

5.2.1 Detector system construction

To represent the real experiment in simulation each component is simplified in order to save computation time and minimise the complexity of the program. The basic components of the measurement setup (target, ALPIDE sensors and the scintillator) are represented by a simple shaped box with the corresponding dimensions (see figure 5.1).

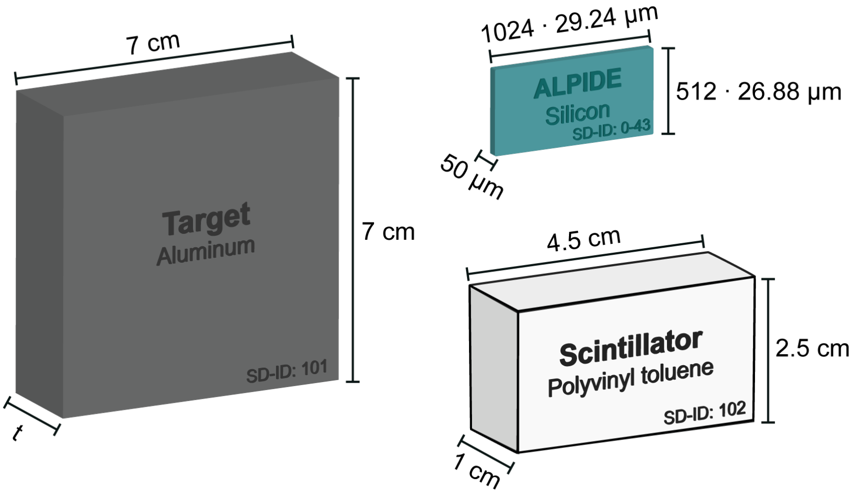

Figure 5.1: Visualisation of the logic volume building blocks of the simulation (not to scale) containing the solid geometry dimensions, with the corresponding material and sensitive detector identification number (SD-ID).

Since the hit position in local coordinates is not of interest, representing detectors only by their sensitive area without any pixelation is sufficient. The target dimensions are chosen such that mounting it on the carrier card of the ALPIDE is possible. Additionally, this choice guarantees that the entire active area of the ALPIDE is covered. The target thickness t is an important parameter, as it influences the rate of reactions and possibly renders low energy measurements impossible (see section 5.5). Therefore the thickness is variable and can be changed using macro files.

The single ALPIDE sensors are thinned down to 50 µm. The sensors integrated in the OBM of the ALICE detector are 100 µm thick [2]. However, the type of sensor integrated into the specific OBM for educational purposes has not been definitively determined at this stage. Consequently, in the simulation, the OBM are currently represented using 50 µm thick ALPIDE sensors, although this choice might require revision in the future.

The materials of these building blocks are chosen such that they represent the materials of the real objects used in a future testbeam as realistically as possible. The target, which consists of pure aluminium, can be easily represented since elements are already implemented as materials. The scintillator is made of Polyvinyltoluene (EJ-200) [20]. The ALPIDE material is more complex as it consists not only of doped silicon but also includes additional metal layers on top for the readout electronics. Thus the material is approximated with pure silicon for simplicity. These basic components are placed inside a world volume that consists of air.

The Outer Barrel Modules (OBMs) include 14 chips divided into two sets of seven sensors placed with a distance in the order of 100 µm to each other. The precise size of the gap is yet to be determined at this stage and it will necessitate adjustments once the information becomes available. A conceptual illustration of one OBM representation in the simulation is shown in figure 5.2.

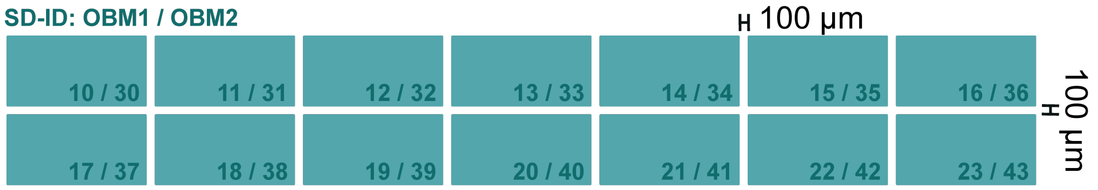

Figure 5.2: Schematic illustration of one Outer Barrel Module (OBM) build from 14 ALPIDE chips with their corresponding ID in the simulation (not to scale).

The spacing of the detector planes is assumed from the experience of previous measurements and optimised to achieve the largest possible acceptance range. A schematic of the whole setup is shown in 5.3. The largest acceptance is achieved by minimising the distances of the detector planes in the measurement telescope. For that reason, the single ALPIDE sensors are placed as close as possible to each other and the target, given the mounting mechanics in the telescope. For the OBM spacing, no experience in previous measurements is available, therefore precautionary 3 cm where chosen.

Each physical volume is assigned to an individual identification number (SD-ID) that is later on used to identify the origin volume of hits.

In the simulation, the detectors are assumed to be perfectly aligned in the x and y dimensions. However, in a real experiment, achieving such perfect alignment is not feasible. Based on past experience, a manual alignment precision of 0.5 - 1 mm can be achieved.

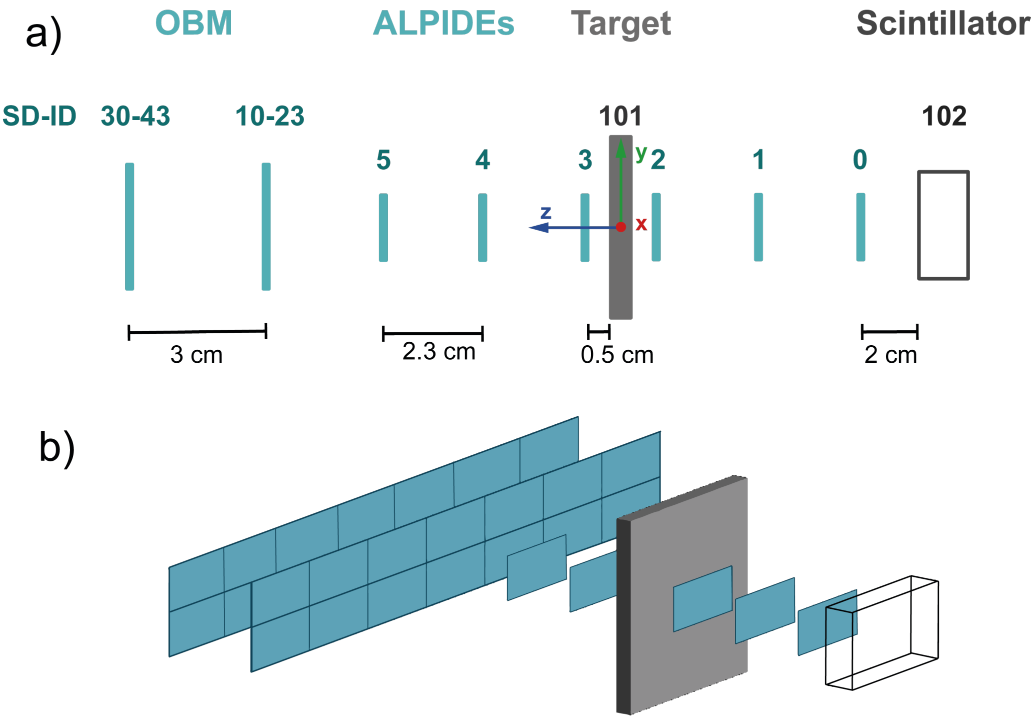

Figure 5.3: Sketch of the simulation setup with distances between planes viewed from the side (a). The numbers above each plane denote the sensitive detector identification (SD-ID). The coordinate system is centred at the midpoint of the target, with the z-axis denoting the beam axis. A three-dimensional visualisation of the setup (b).

5.2.2 Applied physics models

Accurate representation of physics in simulations is essential and critical. Relevant physical interactions must be selected carefully to ensure that important aspects are well represented without requiring extensive computation time. The most important interactions for this thesis are elastic and inelastic hadronic interactions, as well as electromagnetic interactions (see chapter 1).

In section 4.2 the implementation of interactions as physics processes is described. It is explained when they are activated, how the properties of the particles change and how secondary particles are considered. However, the description of the actual process is still missing. A model is needed to describe what happens e.g. in an intranuclear cascade inside the nucleus. The model should provide the change of properties of the primary particle and the amount, type and energy of secondary particles. A process is comprised of both cross-sections and interaction models [38]. Various interaction models exist for specific interactions and the most suitable needs to be chosen and composed in one physics list.

The `QBBC` physics list was selected as it provides the most appropriate description of hadronic inelastic interactions for the protons considered in this study. The processes included in this list and the model employed for inelastic interactions will be described in what follows to clarify why this list was preferred over other available options.

Hadronic component

The hadronic component of the selected physics list includes elastic, inelastic, and capture processes [38]. For proton-nucleus inelastic interactions within the energy range of 0 to 1.5 GeV, the Binary cascade model is utilised [38]. This particular model choice serves as the primary motivation for selecting the `QBBC` physics list over the Geant4 default physics list, denoted as `FTFP_BERT`. The latter, instead of incorporating the Binary cascade, employs the Bertini intranuclear cascade model for protons below 1 GeV [37].

The Bertini cascade model treats a nucleus as a gas of individual nucleons to simulate the cascade. To ensure the validity of this model, traditionally the de Broglie wavelength of the projectile proton should be comparable to the distance of nucleons in the target nucleus. This condition is satisfied for kinetic energies above approximately 200 MeV [18]. However, since the energy range of interest predominantly lies below this threshold, another model was considered to serve the correct representation at low energies. The Binary cascade model is based on a three-dimensional model of the nucleus and exclusively uses binary scattering between primary or secondary particles and the nucleons in the target [22]. Thus, it is typically applicable for much lower kinetic energies starting from a few MeV up to a few GeV.

Recent developments have shown that the Bertini cascade model can be applied to protons in the energy range of 0 to 10 GeV, extending its traditional range [48]. This is noteworthy because the Binary cascade model initially seemed more suitable for representing inelastic interactions at low energies, considering the assumptions of the Bertini cascade model. However, considering the best agreement for thin target experiments in the energy range below 1 GeV, the `QBBC` physics list was ultimately chosen [38].

Electromagnetic component

The electromagnetic part of the `QBBC` physics list includes the standard Geant4 electromagnetic processes. It covers all interactions important for this work. An overview of the interactions that are considered can be found in the reference [21].

The `QBBC` physics list also includes decays of hadrons and leptons. A comprehensive description of the physics list, including detailed information about the parameterisations of the cross-sections used, can be found in the reference [38].

5.2.3 Sensitivity

At this stage, the measurement setup is reconstructed in geometry and the important physics processes are implemented. The remaining task is to build a system that registers hits and acquires data. To simplify the implementation, a single instance of the `G4VSensitiveDetector` class is used to handle the sensitivity of the entire measurement setup. Each physical volume (ALPIDE sensors, target and scintillator) is assigned to an unique identification number (SD-ID) and linked to the sensitive detector class. This allows hits to be traced back to their origin volumes, and specific sensing can be implemented for each volume type.

To provide a clearer illustration of this system, consider a particle propagating through the setup. The `ProcessHits` method is called every time a step is taken in any of the associated physical volumes. So if the particle enters the scintilltor, this method will be called the first time. The SD-ID is examined to invoke the functionality specific to the scintillator. For each step inside the scintillator this functionality is executed. After leaving the scintillator, the particle will trigger the `ProcessHits` method again while entering the first detector. This time the SD-ID of the ALPIDE is registered and the ALPIDE-specific functionality is invoked. The functionality of each sensing volume and the quantities saved are explained in the dedicated section.

5.2.4 Particle beam generation

Accurate modelling of the proton beam is essential to get a precise representation of very important background effects. In this study, the primary protons are generated using the `G4GeneralParticleSource` (GPS) class. At first, the GPS is initialised with the predefined proton particle definition. The momentum direction is aligned with the z-axis and the kinetic energy is set to a default value of 232 MeV. Later on, the energy can be controlled using macro files to allow for energy variation between runs.

The GPS enables the generation of primary particles in a beam-like fashion, with a spatial distribution following a Gaussian profile. The Full Width at Half Maximum (FWHM) is determined based on the capabilities of the possible facility. It is expected to be around 1 cm at the position of the experiment. The beam profile measured on the first detector plane can be seen in figure 5.4.

The choice of a constant beam energy in the simulation is based on the lack of specific information regarding the energy distribution for the considered facility. Although similar medical facilities typically have an energy dispersion of $\Delta E/E < 0.7\%$ [34], the effects of small fluctuations in energy are expected to cancel each other out, supporting the assumption of a constant energy as a reasonable approximation. Nevertheless, this dispersion will be taken into account in further calculations to achieve a more accurate treatment of uncertainties arising from the beam energy.

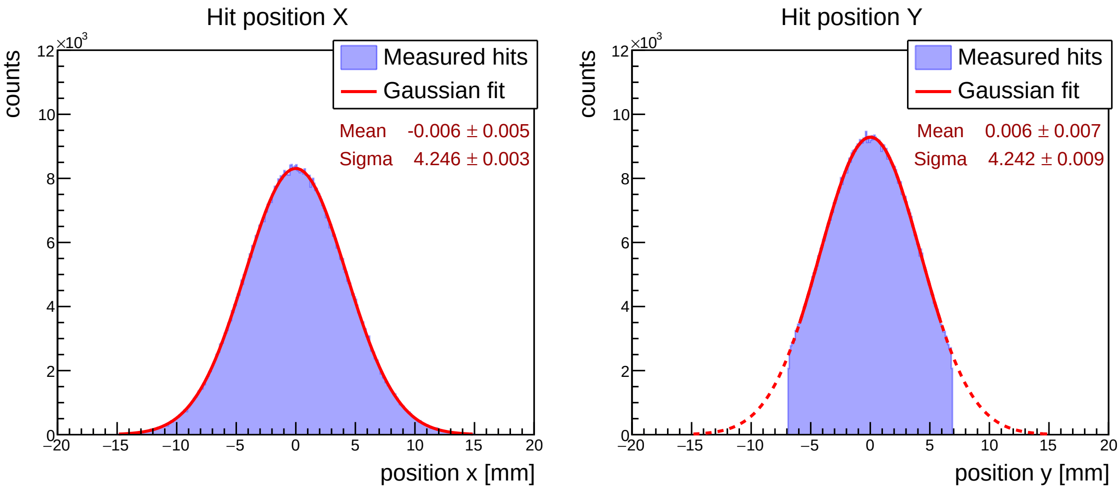

Figure 5.4: Hit positions on the first ALPIDE plane in x (left) and in y (right). A Gaussian fit is applied in the range represented by the solid red line.

5.3 Validation with measurement data

To ensure an accurate representation of the reaction cross-section, a comparison between the Geant4 prediction and available measurement data is made. The measurement data are from previous experiments and are tabulated in [10]. To conduct this comparison, the ALPIDE telescope and scintillator are temporarily removed and the beam start is moved closer to the target to eliminate side effects.

At the same time, a target thickness must be selected. Therefore, a brief evaluation is done to guide the decision. The target thickness has two main influences during this validation. With thick targets, there are more interactions because there are more atoms along the path to interact with. This leads to a reduction in the number of events needed to achieve a good statistical uncertainty, thereby reducing the overall run time. However, using a thick target makes it impossible to compare the cross-section at low energies. The energy loss due to ionisation becomes significant to the extent that it greatly increases the uncertainty of the reaction energy, making it impossible to compare with measured data. A detailed assessment of the effect of target thickness on the measurement is provided in section 5.5. A target thickness of 1 mm was identified as the most appropriate compromise in this case.

Counting incoming particles and inelastic interactions

The key quantities of interest are the number of incoming particles and the number of particles undergoing inelastic interactions (as defined by equation 3.8). The stepping mechanism is used to obtain these values. Since the target is also linked to the sensitive detector class, each step taken within it triggers the `ProcessHits` method. This method is used to count incoming particles and detect inelastic interactions, as described in what follows.

Incoming particles are counted by first checking if the particle is a primary proton. This check is important to exclude secondary particles (e.g. proton coming from reaction in front of the target) from the counting. This is achieved by examining the particle definition and origin volume to confirm that the particle is a primary proton originating from the beam. Next, to ensure that the particle is counted only once as incoming, the pre-step point is checked to determine if it is located at a geometric boundary. Without this condition, the count of incoming particles would increment for each step taken inside the target. Finally, if all three criteria are met, the particle is considered an incoming particle.

Inelastic interactions are counted in a similar manner. The particle is checked to confirm that it is a primary proton. For each step inside the target, it is examined whether the step was triggered by an inelastic process. If this condition is never met, the particle passed through the target without undergoing an inelastic interaction.

Prediction of the simulation

For each event one proton is generated. The number of protons that entered and the number of inelastically interacted protons is accumulated over a run that contains five million events. One run is taken for each energy where a measurement is available. For each run, the reaction cross-section is calculated using a form of equation 3.8

$$\sigma_{\mathrm{R,sim}} = \frac{1}{n_{\mathrm{A}}} \frac{N_{\mathrm{reac}}}{N_{\mathrm{in}}} \tag{5.1}$$

and plotted against the momentum of the primary proton. The corresponding results are depicted in figure 5.5. In comparison, the existing measurements listed in reference [10] are plotted along with their uncertainty.

Since the ratio of two samples, where N_{reac} is a sub-sample of N_{in}, is used to calculate the cross-section, the binomial distribution is used to propagate the uncertainty. The fraction p

$$p = \frac{N_{\mathrm{reac}}}{N_{\mathrm{in}}} \tag{5.2}$$

estimates the binomial probability that a proton that entered the target also interacts inelastically. Note that the discrete probability distribution of the number of reaction events in a sequence of N_{in} independent tests is actually binomial, since there are only two possible outcomes. The particle enters the target and either interacts inelastically or not. Therefore the probability q of entering the target without interacting inelastically is directly obtained by

$$q = 1 - p. \tag{5.3}$$

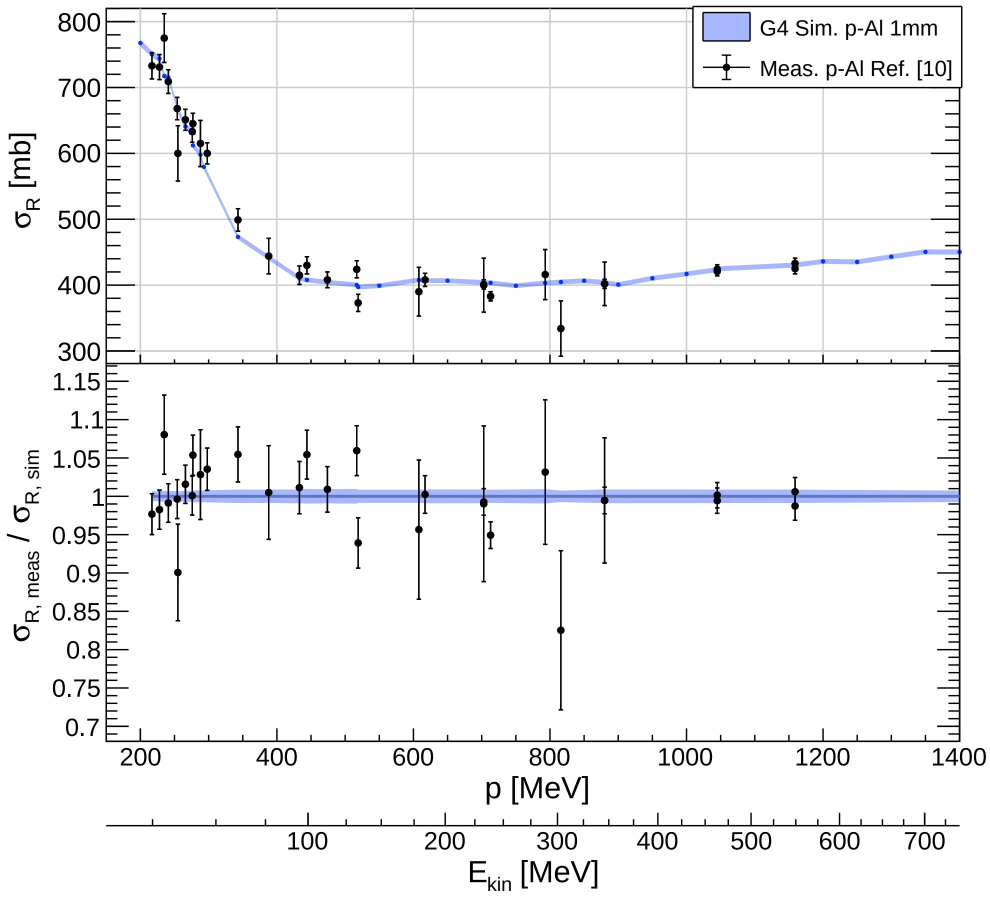

Figure 5.5: Comparison of measured reaction cross-sections (see reference [10]) to the predictions of the Geant4 simulation. The upper plot shows the measured and simulated cross-section as a function of the momentum of the proton. The lower plot shows the ratio of measured and simulated cross-section. In this plot, the error bars represent the uncertainty propagated from the measurement, while the error band visualises the uncertainty propagated from the simulation.

The variance $\mathrm{var}(N_{\mathrm{reac}})$ on the number of reaction events N_{reac} is given by the binomial distribution, as can be found in the literature [36]:

$$\mathrm{var}(N_{\mathrm{reac}}) = N_{\mathrm{in}} \cdot p \cdot q. \tag{5.4}$$

The uncertainty is directly given by the square root of the variance. Therefore the uncertainty of the binomial probability p is derived by:

$$\Delta p = \frac{\sqrt{N_{\text{in}} \cdot p \cdot q}}{N_{\text{in}}} = \sqrt{\frac{p \cdot (1-p)}{N_{\text{in}}}} \tag{5.5}$$

The uncertainty of the reaction cross-section prediction is then derived by dividing it with the number of target nuclei per unit area n_A:

$$\Delta \sigma_{\text{R,sim}} = \frac{\Delta p}{n_{\text{A}}}. \tag{5.6}$$

Quantitative comparison

To enable a quantitative comparison between the simulation and measurements, the ratio of the two cross-sections R:

$$R = \frac{\sigma_{R,\text{meas}}}{\sigma_{R,\text{sim}}} \tag{5.7}$$

is plotted as a function of the momentum in figure 5.5. The uncertainty on this fraction is kept separate for the propagated uncertainty from the measurement and from the simulation. The error bars represent the uncertainty propagated from the measurement, which is calculated by:

$$\Delta R_{\text{meas}} = \frac{\Delta \sigma_{R,\text{meas}}}{\sigma_{R,\text{sim}}}. \tag{5.8}$$

The error bands in this plot show the uncertainty of the ratio propagated from the simulation, which is derived with:

$$\Delta R_{\text{sim}} = \frac{\sigma_{R,\text{meas}} \cdot \Delta \sigma_{R,\text{sim}}}{\sigma^2_{R,\text{sim}}}. \tag{5.9}$$

The comparison reveals a strong agreement between the previous measurements and the simulation. Across the momentum range depicted in figure 5.5, the majority of data points exhibit a deviation of less than $1\,\sigma$, with only a few exceptions. The largest deviation, corresponding to $2.6\,\sigma$, occurs at a momentum of 713 MeV.

The findings presented in this section demonstrate a reliable representation of the reaction cross-section in the simulation. These results indicate the suitability of conducting further investigations on effects related to this cross-section.

5.4 Origin of measurement signatures

The attenuation measurement method assumes that only inelastically interacted particles are removed from the primary beam, while all other protons pass through the target and are measured. However, this assumption is not directly accurate. A variety of effects contribute to the number of particles that are not being measured after the target. Therefore, it is crucial to understand these effects and their frequencies in order to achieve precise measurements and make necessary corrections. This section provides a qualitative insight into the measurement signatures, shedding light on these effects.

In contrast to the validation in the previous section, the number of inelastic interactions can not be directly counted. No logic circuitry is installed that can count if a reaction event occurred. Thus the number of inelastic interactions is inferred from the number of incoming and outgoing protons (see equation 3.8). As a result, the quantities of interest are the number of protons entering the target and the number of particles remaining in the beam after the target.

Definition of tracks

A few definitions and assumptions are made to quantify incoming and outgoing particles. It is important to note that these counts are not only influenced by physical effects, as discussed below, but also by the detection and tracking efficiency, which are neglected in this study.

In the simulation, an incoming track is registered, when the scintillator and all three detector planes upstream of the target are hit, assuming a detection and tracking efficiency of 100 %. Thus, a particle that geometrically intersects these three detector planes automatically is counted as an incoming track.

Outgoing tracks are counted if the particle hits the first plane after the target and at least two more planes. The choice of this definition for outgoing tracks is based on two separate causes. In general, at least three planes are required for sufficient tracking of a particle, as discussed in section 3.3. More complex considerations on the tracking in this experiment might reveal that requiring only two planes could be sufficient by utilising the intersection of the incoming track at the target position as an additional measurement. However, considering only two measurement planes might not work effectively due to the increased probability of uncorrelated hits. The second reason for choosing this definition of outgoing tracks is that a particle trajectory that hits three planes after the target but not the one directly after the target is unphysical within the assumptions of this work. Including the detection efficiency in this consideration can result in such a signature, but it is unlikely.

Registration of tracks

To register hits the `ProcessHits` method checks if the particle is charged and if the pre-step is at the geometric boundary of the sensing volume. Only charged particles are considered since the detection in the silicon sensors relies on energy loss through ionisation. Counting particles only once while entering the sensing volume is ensured by checking the geometric boundary. When a detector is hit, the quantities of interest, namely the hit position and track ID, are stored in a custom hit class object. It is important to clarify that the term ”track” here refers to the Geant4 track object, which contains a unique track ID for each propagated particle in one event. After each event, the hits on all planes are evaluated, and by examining their associated track ID, it is determined whether a single particle propagated through the corresponding planes, thereby counting it as incoming or outgoing. This track ID-based system also enables the detection of multiple outgoing tracks without having to reconstruct the individual trajectories.

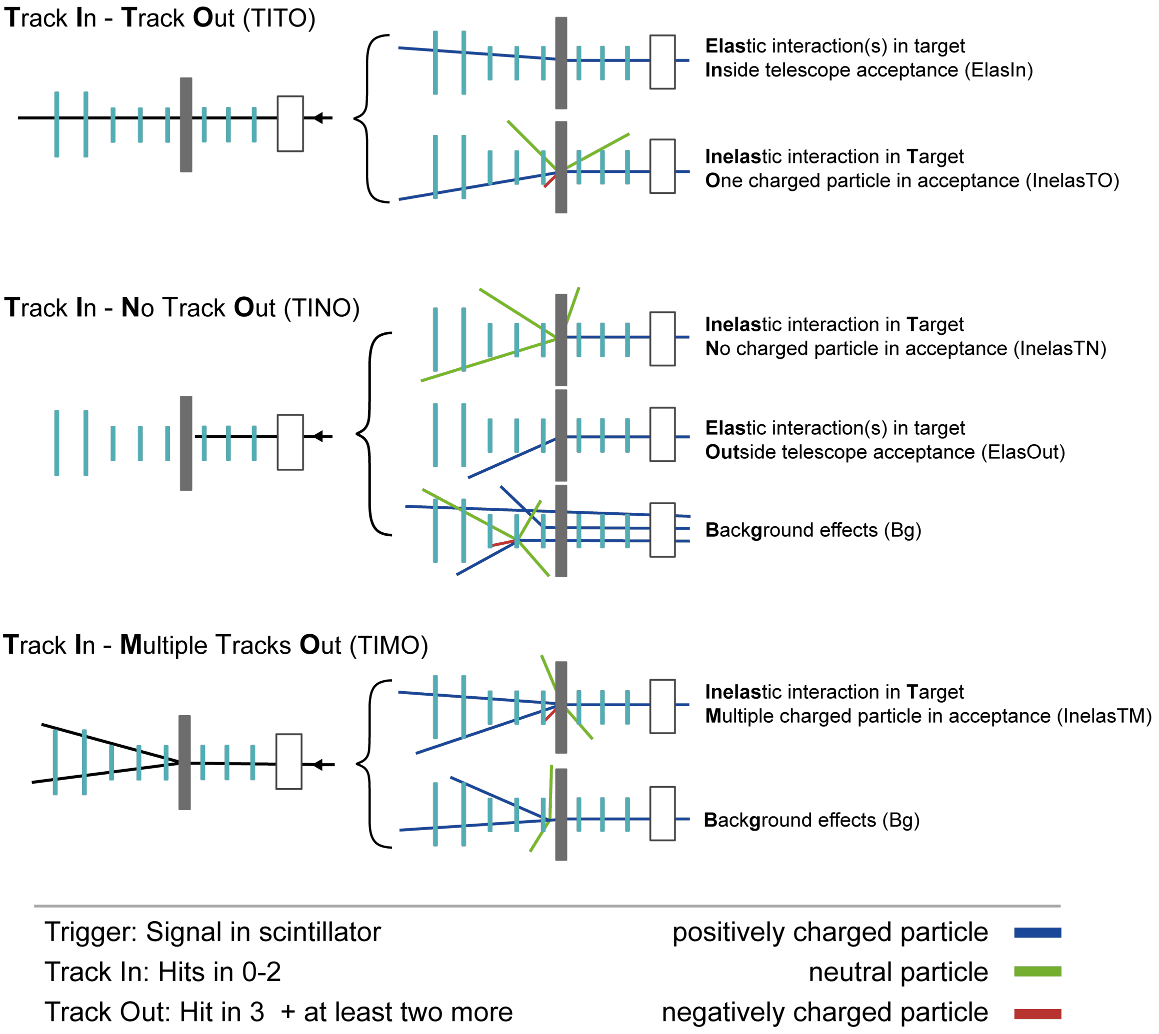

Figure 5.6: Overview of the expected measurement and their origins. Blue lines represent positively charged particles, red ones negatively charged particles and green ones neutral particles.

Classification

Based on these definitions, three main measurement signatures can be identified, which are shown in figure 5.6. Firstly, there are ”track in - track out” events (TITO), where only one track is measured both before and after the target. Secondly, there are ”track in, no track out” events (TINO), where a track is measured upon entering the target but no track is observed after the target. Lastly, there are events where an incoming proton can results in multiple outgoing tracks (TIMO).

These three classes of signatures describe the observed events on the knowledge level of the measurement, but they do not provide information about the underlying causes of these signatures. To gain insight into these event classes, knowledge from the simulation is employed to define and quantify these factors. Due to the multitude of possible events, the classes are simplified to highlight the most significant differences. It is crucial to emphasise that the primary focus lies on interactions within the target, disregarding other effects that have a small probability of happening and do not directly impact the measurement, in order to maintain simplicity.

5.4.1 Track in - track out (TITO)

The attenuation method expects that these events only originate from protons traversing the target without interacting inelastically. Thus, the measured events should exclusively consist of elastic interactions inside the target (ElasIn). Elastic interactions includes three scattering effects: Rutherford scattering, nuclear elastic scattering, and multiple Coulomb scattering. In this case, the scatterings have a small impact on the trajectory of the projectile particle and it can still be measured in the telescope after passing through the target.

The initial expectation that this class predominantly consists of ElasIn signatures holds true for the majority of TITO events. However, the same event signature can also arise from inelastic interactions, where a charged particle can be measured afterwards (InelasTO). This is the case for inelastic scattering of the proton at small angles, where the outgoing charged particle is identical to the incident proton, but the target nucleus is left in an excited state. However, the incident proton might not be present in the final state and instead, a charged secondary particle is emitted from the nucleus.

Certainly, there exist various other events that can produce a similar signature, such as inelastic interactions occurring within a detector with an outgoing charged particle in the acceptance range. However, these events do not impact the measurement as no inelastic interaction in the target is overlooked. Hence, all such events are still classified as ElasIn. This emphasises again, that the class definition is based on what occurs inside the target rather than its surroundings.

To distinguish between these two event classes, the same mechanism as the one used for validation (see section 5.3) is utilised. If an incoming and outgoing track was found it is checked whether an inelastic interaction occurred inside the target or not. The event is classified accordingly.

5.4.2 Track in - no track out (TINO)

According to the attenuation method, this particular class should only include events involving inelastic interactions occurring inside the target (InelasTN). These interactions can lead to various different final states that show the TINO signature. After the reaction, there could be no charged particle existing at all (as illustrated in figure 5.6) or there are one or more charged particles that are not measured as outgoing tracks.

Elastic scattering

Besides the desired signature, there are other factors that can result in a missing outgoing track. One such factor is the elastic scattering of the proton inside the target (ElasOut). In this case, the relevant interactions are the same as for ElasIn, with the difference being that the protons are deflected outside the acceptance of the telescope. Scattering is particularly relevant in the edge regions, where even small deflections of the trajectory can lead to track loss. However, identifying multiple scattering in the target as the sole cause of the missing outgoing track is challenging. If multiple scattering caused by the target would barely keep the particle track within the acceptance region but additional scattering would occur on the detector planes, deflecting the trajectory outside the acceptance, it becomes difficult in the experiment to determine whether the contribution of the target was the main cause for the vanishing track.

To quantify the ElasOut events resulting from multiple scattering in the target, a two-sided approach is chosen. Firstly, a threshold angle θ_{thr} is defined. If the deflection angle exceeds this threshold, the influence of the target is considered significant and the particle is classified as ElasOut. However, this definition alone is insufficient for edge cases, as smaller angles can still lead to a track loss, that is then considered falsely as background. This leads to a systematic overestimation of the background, which is later not corrected by the target-out measurement, resulting in a systematic overestimation of the final reaction cross-section. To address this issue, the incoming tracks are confined to a specific region of interest (ROI). If the particle scatters in the target by an angle below the threshold, it will still be detected per the definition of the restriction. Thus only real background events caused by the surroundings of the target are registered as such. The details of this restriction are discussed in section 5.6.

The choice of the threshold angle has a two-fold impact. A very large threshold would ensure that the target is definitely causing the loss of the track. However, a large restriction on the incoming tracks is needed in this case. This minimises the yield of triggered to measured particles and therefore increases the measurement duration. A very small threshold angle leads to an overestimation of ElasOut events since small scattering angles at the target would falsely be counted as ElasOut events. This results in an underestimation of the reaction cross-section after correcting for these events. As the loss of statistics can be compensated for by a longer measurement duration or higher rate, a fairly large threshold angle is chosen:

$$\theta_{thr} = 3 \cdot \theta_{plane}^{rms} \tag{5.10}$$

The threshold angle is dynamically calculated for each particle using equation 1.5 and the energy registered upon entering the target.

Background

In addition, it is important to consider the presence of various background effects associated with interactions outside of the target that lead to a vanishing outgoing track (Bg). Examples of background events can be seen in figure 5.7. Without taking any measures to mitigate the background, most of it stems from edge-related effects. This is caused by the beam divergence resulting in a large number of particles at the detector edges (see figure 5.4), especially at low energies.

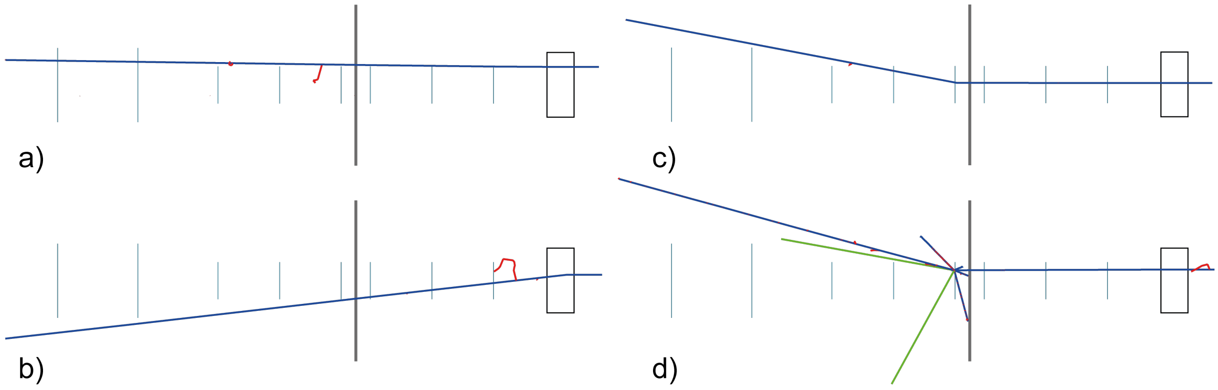

Figure 5.7: Event display of background reaction events viewed from the side. Edge effects such as multiple scattering in target and detectors (a) and divergent tracks from scattering in the scintillator (b) make up for a major part of the background. Note that in a) the particle barely misses the detectors 3-5 and therefore only creates two hits. The remaining background is caused by elastic (c) and inelastic (d) interactions in the detectors.

Particles at the edges pose a challenge as they can be registered as incoming tracks without a corresponding outgoing track due to two distinct effects. Firstly, the scattering within the scintillator can result in highly divergent tracks with large angles (see figure 5.7b) that indicate an incoming particle but lack an outgoing track. Secondly, multiple scattering can easily deflect the proton out of the acceptance region (see figure 5.7a), as even small angles at the edges are sufficient to cause particle loss. Both the detectors and the target contribute to this multiple scattering, as discussed earlier.

Additionally, elastic and inelastic interactions occurring in the detectors after the target contribute to the background (see figure 5.7c + d).

While it is not possible to manipulate the frequency of elastic and inelastic interactions, it is worth noting that these interactions are relatively infrequent. Consequently, the focus lies on minimising edge effects to mitigate the background contribution. A quantitative approach to address and mitigate these edge effects is presented in section 5.6.

To distinguish between these three classes that cause TINO events, the interactions inside the target are analysed once again. If an inelastic interaction is detected, the event is classified as InelasTN. If no inelastic interaction is registered, elastic interactions are examined. Rutherford and nuclear elastic scattering are identified using the same method as used for inelastic interactions. They are implemented as discrete processes invoked at the end of each step, enabling tracking of these interactions by examining the limiting process within the target.

If neither of these interactions occurred, multiple scattering is investigated. However, this is more complex as it is a continuous process. Thus, changes to the particle are applied at the end of each step. To determine if the event signature is caused by multiple scattering, the defined threshold angle is utilised. To apply this threshold criterion the angle of deflection needs to be determined. This is done by registering the momentum direction of the proton while entering and leaving the target. The two vectors are projected onto the xz and yz planes, allowing for individual calculations of deflection in each dimension. Subsequently, the scattering angle in each dimension is compared to the threshold angle. If at least one of them is larger, the event is classified as ElasOut. If neither inelastic nor elastic interactions are observed within the target, the event is attributed to background effects.

5.4.3 Track in - multiple track out (TIMO)

A signature with multiple outgoing tracks is expected to be produced only by inelastic interactions (InelasTM). These events are determined by examining the interactions inside the target and registering inelastic interactions. However, within the assumptions of this study, there is another possibility of producing a second outgoing track. The delta electrons produced in ionisation processes have a probability of hitting three planes after the target, creating an outgoing track as defined in the simulation. This is possible since only the hits on the planes are considered and not the trajectory of the delta electrons. Due to their low momentum, these particles experience large deflections at each detector plane as can be seen in figure 5.8. To illustrate this, the mean multiple scattering angle is calculated for the maximum expected energy of these delta electrons.

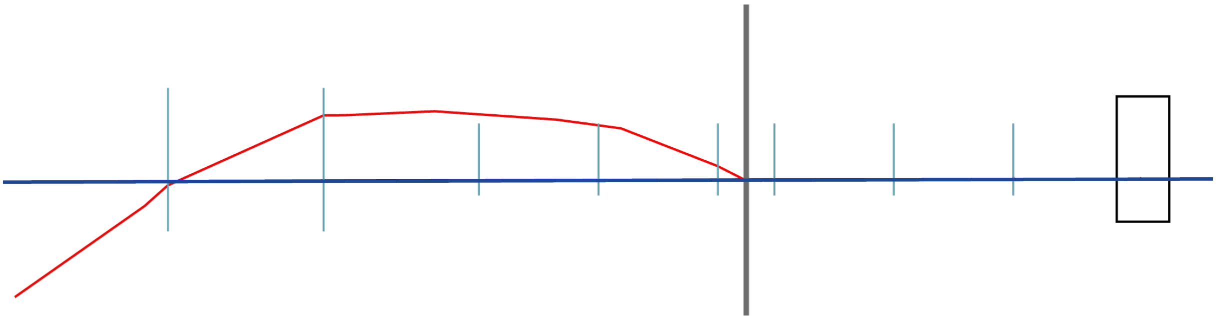

Figure 5.8: Event display of a TIMO event caused by a delta electron produced in the target, as viewed from the side. In the display, the blue line represents the primary proton, and the red line represents the delta electron.

The maximum kinetic energy of the delta electrons is given by equation 1.3. For the maximum kinetic energy of the considered protons (232 MeV), the maximum kinetic energy of the delta electrons amounts to 0.56 MeV. Consequently, the expected scattering angle on the detector planes is calculated to be 430 mrad or 24.6°. This corresponds to a displacement of 1.1 cm for the hits on planes 3 and 4, resulting in completely decorrelated hits. To ensure the exclusion of all delta electrons, a selection criterion was applied, considering only electrons with kinetic energies above 1 MeV. Any electrons below this energy threshold are not considered for outgoing tracks.

In real experiments, the rejection of delta electrons can be achieved by assessing the quality of a straight-line fit. At first, the combinatorics of all hits are considered to determine the proton trajectory by the best χ^2-fit, as it is expected to deflect only slightly. The remaining hits are combined and possible tracks are rejected based on the χ^2-value of the fit. As demonstrated earlier, these low-energy delta electrons are anticipated to exhibit a highly deflected path, leading to a poor fit when attempting to model it as a straight line.

If multiple outgoing tracks are detected in simulation, it is verified whether an inelastic interaction has occurred. If no inelastic interaction is recorded, the event is classified as background (`Bg`). Background events include, for instance, inelastic interactions in the air between the target and the detector, resulting in the production of a second charged particle.

At the end of each event, several quantities are recorded. If the particle successfully hit the scintillator, the event is considered triggered and the count for triggered events is incremented. Additionally, if an incoming track is identified, the corresponding count is incremented. The number of outgoing tracks is determined as described previously. The event is then classified by analysing the observed signature and interactions within the target and the respective class count is incremented. As a result, for each run, a histogram is generated that includes the number of triggers, incoming tracks, outgoing tracks, and counts for each class. To gain knowledge on the relative abundance of the different classes nine runs spread over the energy range of interest with each 50 million events were simulated.

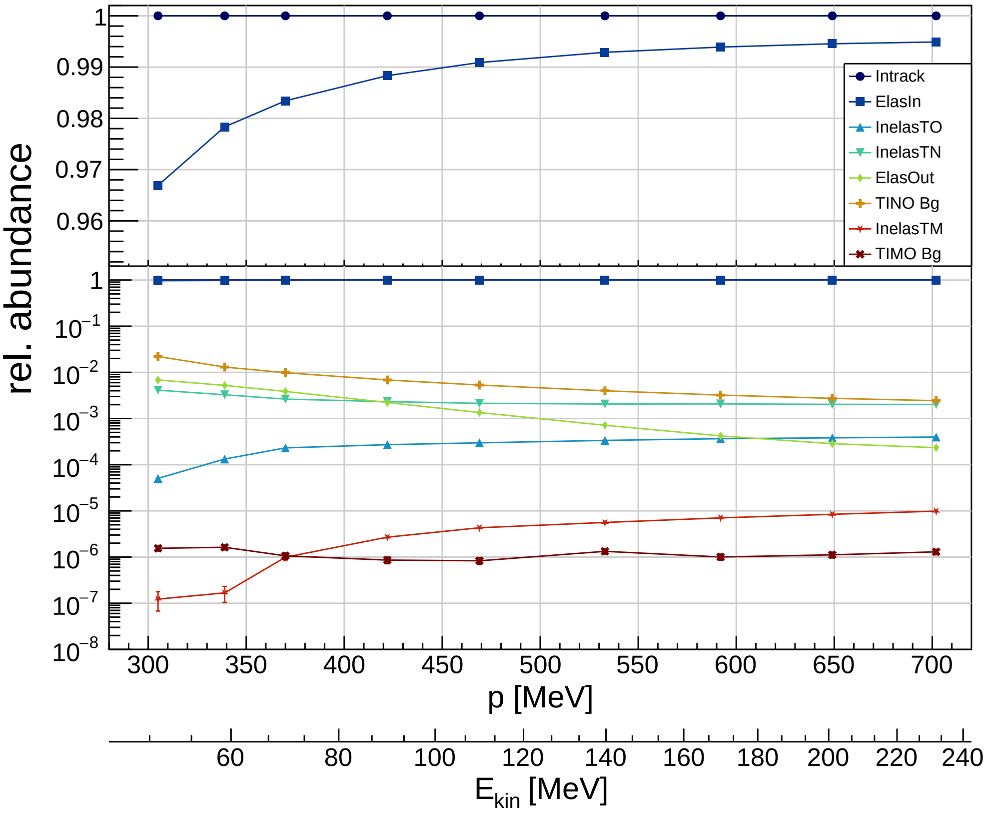

Figure 5.9: Relative abundance of each event class as a function of the proton beam energy using a target thickness of 1 mm. The abundance is calculated as the ratio of counted events in each class to the number of counted events with incoming tracks.

The ratio of the specific events counted in each class to the incoming tracks is calculated and plotted against the momentum of the primary proton. The result is shown in figure 5.9. The uncertainty of this ratio can be calculated again using the binomial distribution since all classes are sub-samples of the incoming tracks. Due to the high number of simulated events, the resulting uncertainty is negligible for most event classes.

The results presented in this plot provide an initial impression of the significant quantities involved in the measurement. They also enable the verification of whether the counts in each class align with the anticipated outcomes based on the underlying physical phenomena.

Evaluation of the class frequencies

The occurrence of ElasIn events dominates the Intrack events and shows an upward trend with increasing energy. This upward trend can be attributed to the declining abundance of TINO events across the energy range, which will be discussed next.

At this stage, without implementing any additional measures, the next significant component is the background (TINO Bg), which tends to overshadow the signal composed of InelasTO, InelasTN, and InelasTM events. The background encompasses various energy-dependent effects. The differential cross-section for Rutherford scattering, being proportional to the inverse momentum of the proton squared, decreases with increasing energy. This impacts two of the major contributors to the background. The reduced cross-section for elastic scattering results in fewer divergent tracks caused by scattering in the scintillator. Moreover, elastic scattering in the detectors after the target is reduced, further contributing to the decline in Bg events. Additionally, the multiple scattering depends on the inverse momentum of the incident proton and therefore decreases as well for increasing energy. Since aluminium and silicon share a similar atomic mass number, a comparable distribution of the reaction cross-section is expected. Therefore, a decrease in the cross-section with increasing energy is anticipated (see figure 5.5). Consequently, the number of inelastic interactions in the detectors after the target is also reduced for higher energies. Although these background events can be corrected with the target-out measurement, minimising their contribution is favoured to reduce the statistical uncertainty introduced by the measurement.

Similarly, the number of ElasOut events decreases with energy, which can be attributed to the dependence of elastic scattering on the energy of the incident proton.
An interesting observation is the intersection of false-positive (ElasOut) and false-negative (InelasTO) events at approximately 580 MeV momentum. This indicates that after background correction, the cross-section will be overestimated for low energies and underestimated for higher energies.

As expected, the abundance of multiple outgoing tracks is very suppressed. This can be explained by the amount of InelasTN events. In most inelastic interactions, the proton is removed from the primary beam, as evident from the disparity between InelasTO and InelasTN events, which differs by approximately one order of magnitude. Either inelastic scattering must occur with minimal deflection of the proton, or the inelastic interaction must involve the emission of a charged particle within a narrow solid angle. As the requirement for two outgoing tracks includes at least one outgoing track from an inelastic interaction, the number of InelasTM events exhibits a slight increase with energy. This is due to the growing number of InelasTO events being observed, which enhances the chances of registering two outgoing tracks.

The thickness of the scintillator increases the possibility of inelastic interactions occurring within it. This might result in a charged particle (that is not the original proton), which is detected as an incoming track. Consequently, there is a chance that the measurement of the reaction cross-section may be contaminated by incoming tracks from unknown particles. For the purposes of this study, it is assumed that the probability of two inelastic interactions happening in a single event is negligible. This assumption is reasonable given that the likelihood of an inelastic interaction in the target is on the order of 10^{-3}, depending on the chosen target thickness. This probability is then multiplied by the probability of an inelastic interaction in the scintillator, which is expected to be slightly higher due to its increased atomic density per unit area compared to the target. However, as depicted in figure 5.9, the majority of inelastic interactions do not result in the presence of a charged particle in the forward direction in the final state. As a result, the probability of contamination from unknown particles becomes even smaller, allowing it to be disregarded.

Consequences for the measurement

This qualitative assessment of the event classes reveals several consequences for the actual measurement. The desired signal for reaction events consists of three components: InelasTN, InelasTO, and InelasTM. However, the latter two components are not accurately identified (false negative events). It should be noted that the contribution from InelasTM is significantly (more than two orders of magnitude) smaller compared to InelasTN, rendering it insignificant. To restore the complete signal after the measurement, it is necessary to consider and account for the false negative events. The abundances obtained in this section will provide valuable knowledge for this purpose.

The initial signal is contaminated by the presence of false positive ElasOut and TINO Bg background events. It is necessary to isolate the true signal from these events. The background can be effectively corrected through a target-out measurement. The frequency of false positive events determined in this section will be used to correct for them accurately.

The key insights from this section are twofold. Firstly, the background component constitutes a significant portion of the events where tracks vanish, highlighting the importance of minimising edge effects to mitigate this background contribution. Secondly, accurate corrections to the initial measurements are essential for obtaining a precise estimation of the reaction cross-section.

5.5 Influence of the target thickness

The selection of the target thickness is a critical decision that impacts the overall uncertainty of the cross-section and reaction energy, as well as the minimum measurable energy. There are several effects associated with the target thickness that need to be considered.

Impact on the reaction rate

From a statistical perspective, a larger number of reactions should be measured to achieve a desirable level of statistical uncertainty. In this regard, a thicker target would be advantageous as it increases the number of possible interaction centers encountered by the protons, resulting in a higher overall interaction rate. This effect can be observed in figure 5.10 (left plot). It should be noted that the lower reaction rate for thin targets can be compensated by increasing the measurement duration or rate, if possible. This is not always the case at testbeam facilities, as usually a limited time is offered.

Impact on the proton absorption

As the target thickness increases, the protons experience a greater amount of energy loss. This leads to an increased probability of proton absorption due to energy loss. Consequently, at sufficiently low energies and for a thick enough target, the contribution of proton absorption becomes significant. It is worth noting that absorption due to energy loss can occur in conjunction with elastic scattering, where the proton scatters in such a way that it traverses more target material, resulting in additional energy loss.

Thickness t [mm]	E_{loss} / E_{in} [%]
5	90 ± 4
4	58.4 ± 1.4
2	24.7 ± 0.7
1	11.68 ± 0.5
0.5	5.70 ± 0.3
0.1	1.11 ± 0.14

Table 5.1: Relative energy loss of protons produced at 48 MeV through the various target thicknesses. E_{in} refers to the energy of the proton upon entering the target. E_{loss} is the mean energy loss expected for the corresponding thickness t. The energy loss through setup and target is calculated with Catima [39].

If an absorption occurs in the simulation, the event is either counted as ElasOut if elastic scattering happened in conjunction or TINO Bg if not. Figure 5.10 (middle plot) illustrates the ratio of false positive reaction events (ElasOut and TINO Bg events) to incoming tracks as a function of the incident proton energy. It is expected that the number of these events increases at low energies due to the dependence of elastic scattering on the proton energy. However, for the 5 mm target at low energies, almost all incoming tracks fail to produce any outgoing track without interacting inelastically. This significant increase is attributed to energy loss and subsequent proton absorption. In order to further examine the contribution of absorption from energy loss the expected mean energy loss in the target is calculated for the lowest kinetic energy using the Catima code library [39].

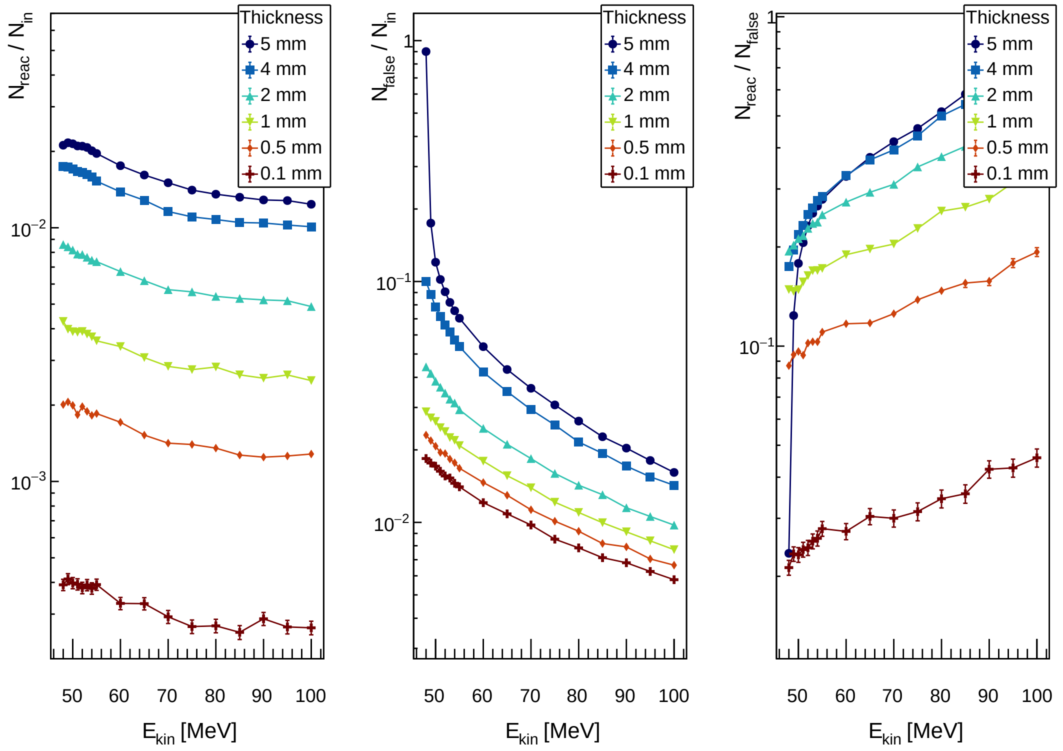

Figure 5.10: The left plot shows the number of reaction events to the incoming tracks as a function of the kinetic energy of the incident proton. The plot in the middle side shows the number of false positive reaction events as well as the ratio to the number of registered incoming tracks. The plot on the right-hand side displays the ratio between the reaction and false positive events for various target thickness.

The results are presented in table 5.1. The thickest target shows a mean energy loss of approximately 90% of the energy it has upon entering the target. Due to the statistical nature of the ionisation, the energy of the proton after the target is distributed. This is known as energy straggling. This straggling is reflected in the uncertainty given in table 5.1. These results show that for a thickness of 5 mm the absorption due to only energy loss becomes probable. This probability is enhanced as elastic scattering in the target can lead to a longer path and therefore even higher energy loss. This phenomenon explains the increase observed in figure 5.10. On the other hand, a thin target with a thickness of 0.1 mm exhibits a mean relative energy loss of only 1%. The table clearly demonstrates that a thin target is preferable for measurements at low energies, as it minimises absorption effects. The thickness also defines the minimum measurable energy as for low energies, absorption can significantly impact the measurement. In principle, the simulation could be used to correct the absorption events. However, this is a correction that introduces unnecessary uncertainty since this effect can be easily compensated by choosing a thinner target.

Impact on the signal to false positive ratio

The middle plot in figure 5.10 reveals another important aspect across the entire energy range. Thicker targets result in a higher number of false positive reaction events, indicating another disadvantage of increasing the target thickness. The possible interaction centers do not only increase for inelastic but also for elastic interactions, leading to more ElasOut events. Correcting for these events becomes necessary, making it favourable to minimise their occurrence and reduce the propagated statistical uncertainty.

In order to determine the optimal compromise between achieving a high reaction rate and minimising the false positive events, the ratio of both is plotted in figure 5.10 (right plot). It can be observed that selecting a very thin target thickness results in a very low ratio of reaction to false positive events. This can be attributed to the nature of the background events, which are uncorrelated to the target thickness and therefore remain constant while varying the thickness. Consequently, reducing the thickness leads to a decrease in the number of reaction events, while the number of background events remains the same. Visually speaking, as the target becomes thinner, the material of the detector telescope becomes more prominent, resulting in an increased relative number of inelastic interactions compared to those occurring in the target.

This observation sets a lower limit for the target thickness. It indicates that for targets thinner than twice the thickness of the ALPIDE (0.1 mm), the background events would completely dominate the signal, without any possibility of mitigation. This factor of two arises from the fact that only inelastic interactions occurring in planes 3 and 4 can give rise to a background event, based on the defined criteria for outgoing tracks. Therefore, to ensure that the signal is not overwhelmed by background events, the target thickness should be at least twice the thickness of the ALPIDE detector.

Impact on the uncertainty of the reaction energy

The reaction energy corresponds to the energy at which inelastic interactions occur. To provide the cross-section for a specific energy, precise knowledge of this energy is required.

With a thicker target, the uncertainty of the reaction energy increases as the spatial range for possible interactions expands. Depending on where the reaction takes place, the proton may have lost varying amounts of energy, resulting in a larger uncertainty for the reaction energy. For very thin targets, it is important to consider the energy straggling effect. In table 5.1, it can be observed that the relative uncertainty of the energy loss increases as the target thickness decreases. This is due to fewer statistically independent collisions and as a result higher fluctuations in the energy loss. However, the absolute energy loss is very small for thin targets and therefore also the absolute uncertainty from straggling. Therefore it is highly likely that these fluctuations are negligible compared to other factors contributing to the uncertainty in the reaction energy, such as beam energy dispersion and energy straggling through the setup in front of the target. For this reason, it is not expected that the uncertainty in the reaction energy will worsen significantly for thin targets. However, the effects of energy straggling should be thought of when estimating the overall uncertainty.

This section highlights the different factors influencing the choice of the target thickness. A thick target offers the advantage of higher reaction rates and as a result a higher ratio of true to false reaction events. On the other hand, a thin target reduces the uncertainty in the reaction energy and allows for measurements at low energies. For this reason, the thickness should be chosen to strike a balance between minimising absorption due to ionisation and achieving the desired reaction energy uncertainty, while also maximising the signal-to-background ratio. This balancing is influenced by the energy at which the measurement is conducted, as the importance of the reaction energy and cross-section uncertainties vary with energy. For kinetic energies above 100 MeV, the cross-section distribution exhibits a relatively flat behaviour. Therefore, the uncertainty in the reaction energy becomes less significant compared to the uncertainty in the cross-section itself. In contrast, at lower energies where the cross-section distribution is rising, the uncertainty in the reaction energy becomes more crucial.

For further investigations, a target thickness of 1 mm was chosen. This decision was based on the vanishing probability of absorption solely due to energy loss, as well as the trade-off between achieving a high reaction rate and maintaining a precise reaction energy uncertainty. It is important to note that while this choice may not be optimal across the entire energy range, it serves as a suitable starting point for future investigations.

5.6 Minimising edge effects

At the edges of the telescope, two distinct effects have a significant impact on the measurement. Firstly, multiple scattering within the target can lead to track losses. Even small deflections can result in the loss of the particle track. Quantifying this effect is challenging, as the amount of deflection required to lose a track depends strongly on the incident position. In section 5.4, it was defined that a track loss is attributed to the target when the multiple scattering angle at the target exceeds a threshold value of $\theta_{thr} = 3 \cdot \theta^{rms}_{plane}$. However, it should be noted that even smaller angles for tracks passing close to the edges can cause track losses, which are then mistakenly classified as background events. Therefore, a solution needs to be devised to address edge effects related to multiple scattering in the target, particularly for angles smaller than the defined threshold.

The second effect is the presence of divergent tracks resulting from scattering in the scintillator material. These tracks generate a significant number of background events. Although they are corrected through the target-out measurement, it is advantageous to mitigate their impact to keep the statistical uncertainty introduced by the background correction as low as possible.

Two potential solutions can address the issues caused by tracks at the edges. The first approach involves using a more focused beam, which centers the particles and reduces the impact of edge-related effects. However, this solution relies on the capability of the facility to produce a more focused beam or to move the experiment closer to the beam exit. The second approach, chosen due to the unknown circumstances at potential facilities, involves confining the incoming tracks to a specific area on the detectors. By restricting the tracks in this manner, the disadvantageous effects of divergence and multiple scattering with angles smaller than the defined threshold can be minimised. The restriction of incoming tracks is designed to ensure that even in the extreme case of the most divergent track possible and the largest scattering angle $\theta_{\max} = \theta_{thr}$, the particle will still be detected downstream. This discussion focuses on the lowest considered energy, as the same principle applies to higher energies, but there the deflection is smaller.

Calculation of the restrictions

The calculations for the restriction in each dimension are visualised in figure 5.11. Here, the calculation for the x-dimension will be shown exemplary, noting that the same procedure applies to the y-dimension. The approach involves constructing two straight lines, namely $f_1(z)$ and $f_2(z)$, which represent the incoming and outgoing tracks, respectively. These lines can be described by the equations:

$$f_1(z) = m_1 \cdot z + c_1 \qquad f_2(z) = m_2 \cdot z + c_2 \tag{5.11}$$

For the calculation of the restriction in the x-dimension, two points, $p_{1,x}$ and $p_{2,x}$, are defined to represent the restriction:

$$p_{1,x} = \begin{pmatrix} x_{\text{res}} \\ 0 \\ z_0 \end{pmatrix}, \; p_{2,x} = \begin{pmatrix} -x_{\text{res}} \\ 0 \\ z_2 \end{pmatrix}. \tag{5.12}$$

Here, x_{res} represents the desired restriction with respect to the middle of the sensor, while z_0 and z_2 denote the z-locations of the 0th and 2nd detector, respectively.

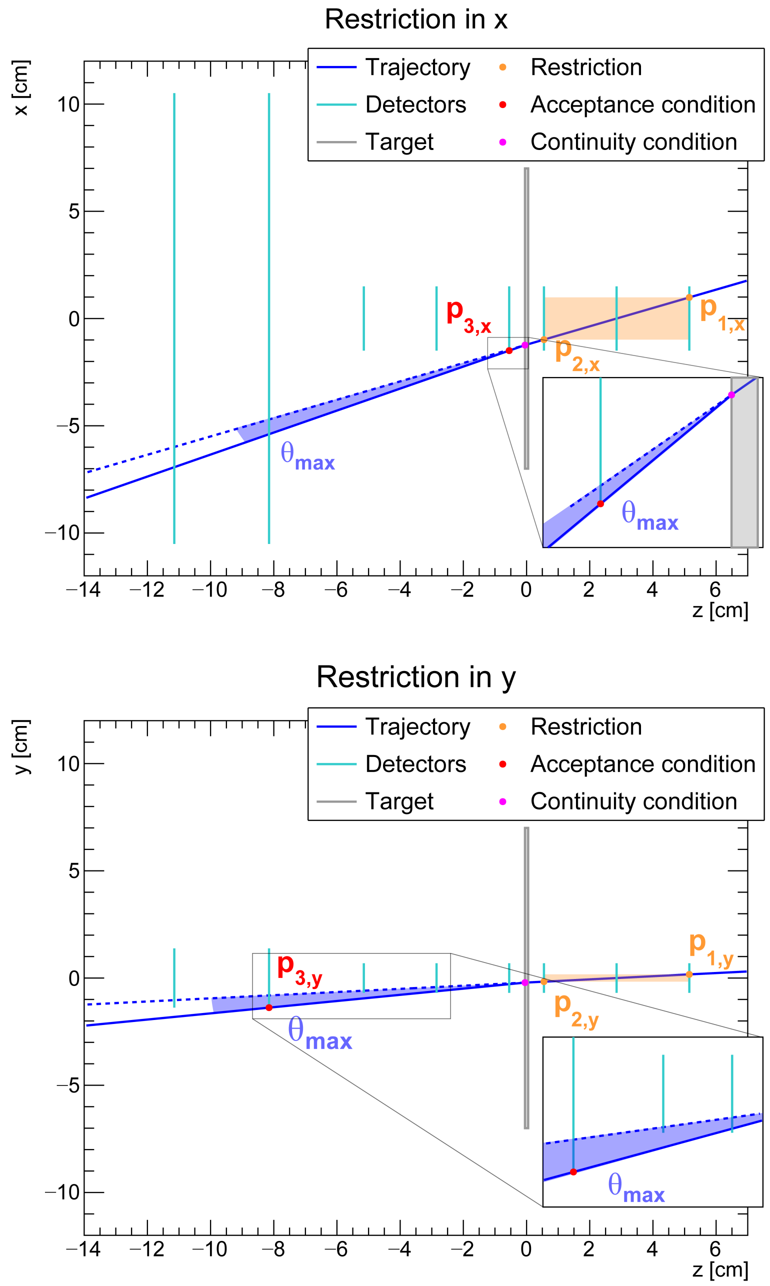

Figure 5.11: Visualisation of the geometrical calculation to determine the restriction of incoming tracks in x (top) and y (bottom) dimension (to scale).

Assuming that all incident angles are possible, the first line passes through $p_{1,x}$ and $p_{2,x}$ in the case of extreme divergence. From this condition, the first line $f_1(z)$ can be constructed using the following parameters:

$$m_1 = \frac{2x_\mathrm{res}}{(z_0 - z_2)} \text{ and } c_1 = \frac{-x_\mathrm{res}(z_0 + z_2)}{(z_0 - z_2)}. \tag{5.13}$$

To determine the parameters of the second line as a function of the restriction x_res, another system of two equations is required. The first condition ensures that the outgoing track intersects with the incoming straight line at the target position, and the second condition fixes the angle between the two straight lines to represent the maximum multiple scattering angles that should keep the particle trajectory within the acceptance.

The first condition neglects the offset introduced by multiple scattering in the target. This assumption can be validated by considering the possible offset. Using equation 1.6, the rms of the offset distribution is calculated to be 13 µm for the lowest proton energy considered. Therefore, if the offsets were considered, there would not be a continuity expected at the target edge, and the outgoing track would be offset by 13 µm. Thus, the incoming track would need to intersect the target edge at a higher position to account for the offset. It can be calculated that the change in the restriction to achieve this is expected to be approximately 0.3%, making such a small offset insignificant.

Solving this second system of equations yields the slope and offset of the outgoing straight line:

$$\begin{aligned} m_2 &= -\frac{m_1 + \tan(\theta_\mathrm{max})}{m_1 \tan(\theta_\mathrm{max}) - 1} \\ c_2 &= \frac{c_1 m_1 \tan(\theta_\mathrm{max}) - c_1 + \frac{t}{2} m_1^2 \tan(\theta_\mathrm{max}) + \frac{t}{2}\tan(\theta_\mathrm{max})}{m_1 \tan(\theta_\mathrm{max}) - 1}, \end{aligned} \tag{5.14}$$

where t is the target thickness. It should be noted that by substituting m_1 and c_1, the parameters for the second straight line become dependent on only one parameter, the restriction x_res. Thus, an additional constraint is needed to determine the restriction. For this purpose, a third point, $p_{3,x}$, is defined to set the limitation of the acceptance. Neglecting scattering at the detector planes, the particle needs to pass through the first detector plane after the target in order to be measured in the x-dimension. Therefore $p_{3,x}$ is defined as:

$$p_{3,x} = \begin{pmatrix} h_x \\ 0 \\ z_3 \end{pmatrix}, \tag{5.15}$$

where h_x is half the matrix size of the ALPIDE sensor in the x direction, and z_3 is the position of the detector plane 3. By using the equation for $f_2(z)$ and constraining it to

$p_{3,x}$, the restriction can be determined.

For the y-dimension, a similar calculation can be performed. The only difference lies in the acceptance restriction, as in this dimension, the acceptance is limited by the first OBM. In figure 5.11 (bottom), it can be observed that when the particle hits this OBM, the sensors on planes 3 and 4 are also hit, creating an outgoing track. Therefore, in this case, $p_{3,y}$ is defined as:

$$p_{3,y} = \begin{pmatrix} 0 \\ h_y \\ z_6 \end{pmatrix}, \tag{5.16}$$

where h_y is half the matrix size of the OBM in the y direction, and z_6 is its position.

By applying this calculation, a restriction is obtained that takes into account very divergent tracks and strong multiple scattering in the target. The obtained restrictions are:

$$\boxed{x_{\text{res}} = 9.8\text{ mm} \qquad y_{\text{res}} = 1.7\text{ mm}}$$

In principle, the restrictions could be applied with the precision of pixel on the ALPIDE sensor. However, it is not practical to enforce such high precision as the calculated restriction cannot be determined with that level of accuracy. In the calculation, various statistical effects, such as the energy loss through the first part of the telescope are involved in the calculation. This implies that for each individual proton, the calculation would yield a slightly different restriction. Therefore, it is more sensible to overestimate the restriction slightly, limiting the area more than necessary, rather than risking it being too loose.

Consequences for the measurement

With these restrictions, only a fraction of the total x and y dimensions of the ALPIDE detector is allowed for incoming tracks, approximately 63 % in x and 25 % in y. This significant difference is due to the large coverage provided by the OBM, as illustrated in figure 5.11 (top). The allowed area for incoming tracks represents approximately 16 % of the total area of an ALPIDE detector. This results in a decrease of statistics by about one-fourth. To apply the restriction, the hit positions are evaluated when searching for incoming tracks. Only hits within the region of interest defined by the restrictions are considered and evaluated. This exclusion of hits outside the restriction eliminates particles that have too divergent tracks and miss the valid area on any of the planes in front of the target.

In real experiments, these restrictions are implemented through the use of a region of interest (ROI) in the data analysis. Initially, the data is collected without any specific selection. During the analysis stage, a specific region on the ALPIDE can be defined and only hits within this defined region are selected for further analysis.

It is crucial to emphasise that the case considered for calculating the restriction is highly improbable in the real experiment. The particle not only needs to be produced in the outer region of the beam profile but also needs to scatter at larger angles in the scintillator and additionally scatter in the target with an large angle that is found in the tails of the scattering distribution. The probabilities of these events occurring simultaneously are extremely low. Therefore, the scattering at the detector planes after the target is not taken into consideration, as the probability of such events is even smaller.

A small remark regarding the calculation should be added. In the previously mentioned considerations, it is assumed that the telescope is perfectly aligned, as is the case in the simulation. However, in a real measurement, this is not the case. Therefore, when calculating the ROI, it is important to also take into account the specific alignment of the sensors.

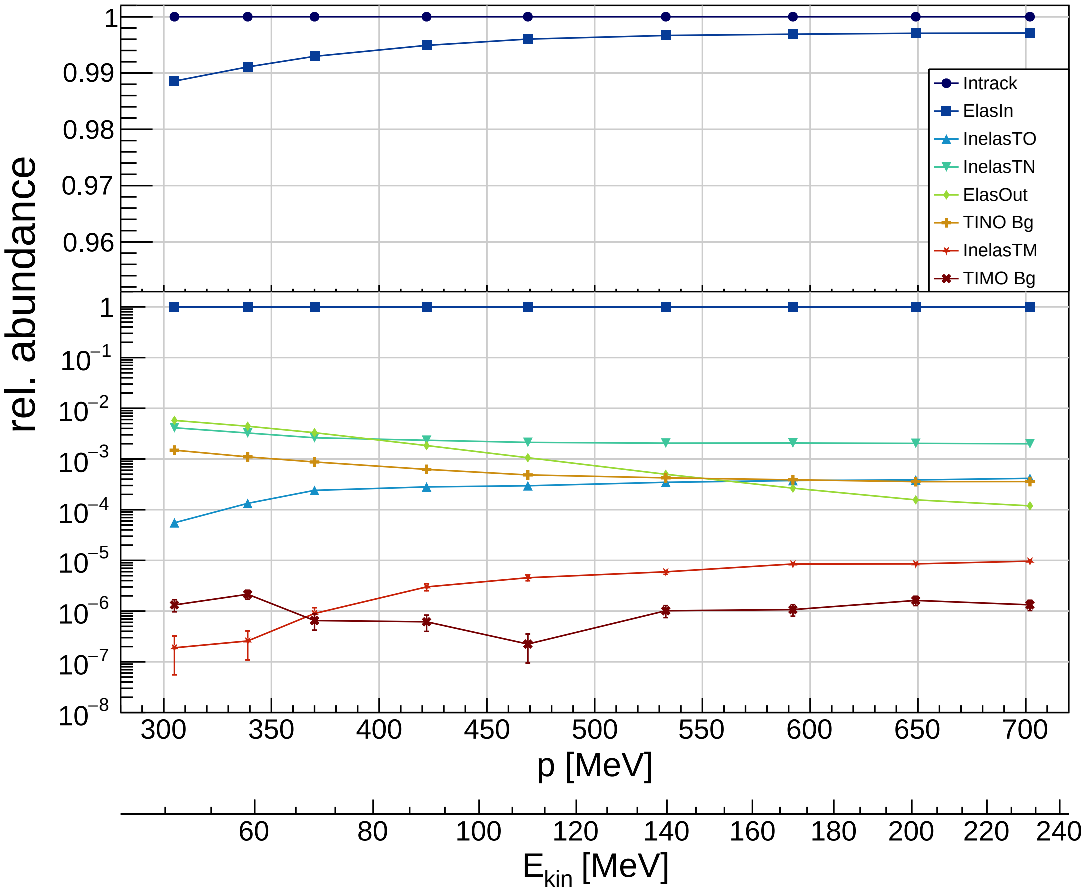

Figure 5.12: Relative abundance of each event class as a function of the primary proton momentum using a target thickness of 1 mm using restricted incoming tracks. The abundance is calculated as the ratio of counted events in each class to the number of counted events with incoming tracks

It should be noted that calculating the restriction for each measured energy increases the yield of events with incoming tracks from the triggered events. This approach adjusts the restriction to be less stringent for higher energies, thereby increasing the number of incoming tracks.

To assess the impact of the restriction, the abundances of the measured signatures are re-evaluated and presented in figure 5.12. It is evident that the background contribution has decreased by an order of magnitude across the entire energy range. As a result, the background now falls below the signal contribution. This demonstrates that the implemented restriction successfully reduces the background. Additionally, a slight reduction in the ElasOut contribution can be observed. This can be attributed to the fact that a larger scattering angle is required to exit the acceptance range within the restricted area, making it slightly less probable.

This section discussed the crucial restriction of incoming tracks, which effectively mitigates background events and addresses the edge effects caused by multiple scattering in the target. By applying the restriction, the impact of multiple scattering in TINO events can be quantified. The restriction ensures that if the target induces a significant scattering angle, the track loss will be accounted for as ElasOut. If the contribution is lower, it is expected that the particle remains within the measurement acceptance. Therefore, if the outgoing track is still absent, it indicates the occurrence of another effect, classifying the event as a background event. Using the restriction calculated in this section, the virtual execution of the measurement can be performed to assess whether the assumptions made result in an accurate measurement of the reaction cross-section.

5.7 Virtual measurement

After thorough preparation, a virtual measurement is carried out with two primary objectives. Firstly, it aims to evaluate the completeness of the assumptions and knowledge acquired in the previous sections, thereby determining their effectiveness in enabling accurate measurements of the reaction cross-section. This evaluation serves to validate the classification and correction methods employed. Secondly, if the initial objective is accomplished, an analysis chain is established that allows to study parameters of the measurement and observing their direct influence on the final result of the measurement.

To cover the entire energy range, nine specific energy values were chosen to reflect the behaviour across a broader spectrum. For each energy, a sample of ten million measurement events was generated. To correct this measured data another sample of 50 million events is generated. From now on ”measurement” refers to the virtually conducted experiment and ”simulation” to separately generated data used for correction.

5.7.1 Correction of background

To account for background events, the target-in-target-out method is employed. This method involves conducting an additional measurement for each energy with the target removed. Since the background events are assumed to be unrelated to the target, this measurement allows for the estimation and correction of background effects.

To ensure consistency, the beam energy is adjusted to match the energy of the protons downstream from where the target would have been. This adjustment is necessary because background effects can vary with energy. The required change in beam energy is calculated individually for each energy using the Catima code library, which calculates the energy loss through the experimental setup [39]. By tuning the beam energy, the energy of the proton at the position where the target would be is made equal to the energy the proton has after passing through the target in the first measurement. This adjustment ensures that the background measurement is comparable to the target measurement, facilitating accurate background subtraction.

The target-out measurement is done with the same amount of statistics. To correct the initial measurement for background events the formula 3.8 needs to be modified to:

$$\sigma_{\mathrm{R}} = \frac{1}{n_{\mathrm{A}}} \left[\left(\frac{N_{\mathrm{in}} - N_{\mathrm{out}}}{N_{\mathrm{in}}} \right)_{\text{target-in}} - \left(\frac{N_{\mathrm{in}} - N_{\mathrm{out}}}{N_{\mathrm{in}}} \right)_{\text{target-out}} \right] . \tag{5.17}$$

Here, N_{in} and N_{out} refer to the number of incoming and outgoing tracks registered. The indices on the brackets distinguish between the target-in and target-out measurements.

The ratios represent the probability that an incoming track will not be observed after the target in both scenarios. As discussed in section 5.4, a missing outgoing track with the target included is not only caused by inelastic events but by a variety of effects, where one of them is background events. To eliminate the contribution of the background events, the probability of a missing track without the target is subtracted from the total probability. To calculate the uncertainty of this corrected reaction cross-section the equation 5.17 can be reformulated to:

$$\sigma_{\mathrm{R}} = \frac{1}{n_A} \left[\left(\frac{N_{\mathrm{out}}}{N_{\mathrm{in}}} \right)_{\text{target-out}} - \left(\frac{N_{\mathrm{out}}}{N_{\mathrm{in}}} \right)_{\text{target-in}} \right] . \tag{5.18}$$

As N_{out} is a direct sub-sample of N_{in}, the binomial distribution can be used again to calculate the uncertainty. In this case, the binomial probability p is defined as:

$$p_{\text{target-in/out}} = \left(\frac{N_{\mathrm{out}}}{N_{\mathrm{in}}} \right)_{\text{target-in/out}} , \text{ with } \Delta p_{\text{target-in/out}} = \sqrt{\frac{p_{\text{target-in/out}}(1 - p_{\text{target-in/out}})}{N_{\mathrm{in}}}} \tag{5.19}$$

for target-in and target-out respectively. Since the two measurements are independent and thus uncorrelated to each other, Gaussian error propagation is used to calculate the uncertainty of the cross-section:

$$\Delta\sigma_{\mathrm{R}} = \frac{1}{n_{\mathrm{A}}}\sqrt{\Delta p^2_{\text{target-out}} + \Delta p^2_{\text{target-in}}} \tag{5.20}$$

5.7.2 Correction of false positive and false negative events

To correct the measurement for false positive and false negative events, the classification of section 5.4 is used. The simulation data is used to determine the expected probability p_x for each class x that has to be corrected:

$$p_x = \frac{N_x}{N_{\mathrm{in}}}, \text{ with } \Delta p_x = \sqrt{\frac{p_x(1-p_x)}{N_{\mathrm{in}}}}. \tag{5.21}$$

These probabilities are then used to correct the measured number of outgoing tracks for the target-in measurement. The number of outgoing tracks, after applying background correction, includes contributions from ElasIn, InelasTO, and InelasTM. However, the latter two, being inelastic events, are not expected to generate an outgoing track. Therefore, the contributions from InelasTO and InelasTM need to be subtracted from the outgoing tracks. Although it was demonstrated in section 5.4 that the InelasTM events are relatively small compared to other signal contributions, they will still be corrected for in the analysis, as the required knowledge is present. The outgoing tracks miss the ElasOut events, which are expected to be measured. Thus, the ElasOut events need to be added to the outgoing tracks.

The corrected number of outgoing tracks is given by

$$N_{\text{out,corr}} = N_{\text{out}} - N_{\text{in}}(p_{\text{InelasTO}} + m \cdot p_{\text{InelasTM}} - p_{\text{ElasOut}}), \tag{5.22}$$

where m denotes the mean multiplicity of multiple charged outgoing tracks. The mean multiplicity was determined from a large data set of 50 million generated events to be

$$m = 2.018 \pm 0.006.$$

The corrected outgoing tracks $N_{\text{out,corr}}$ are used to calculate the corrected binomial probability:

$$p_{\text{target-in, corr}} = \frac{N_{\text{out,corr}}}{N_{\text{in}}} = p_{\text{target-in}} - (p_{\text{InelasTO}} + m \cdot p_{\text{InelasTM}} - p_{\text{ElasOut}}). \tag{5.23}$$

The first term represents the measured probability of an outgoing track whereas the second term corrects this probability with the simulation. Hence, these two terms are uncorrelated.

Since the individual probabilities p_x of the different classes are expected to be correlated with each other (as the sum of all classes must equal one), calculating the uncertainty of $p_{\text{in, corr}}$ becomes a more complex task. Quantifying these correlations is challenging because all the other classes are also involved, and there is no direct physical explanation for how changes in one class impact the others. To simplify the analysis, the individual probabilities are assumed to be uncorrelated. Although this assumption leads to an overestimation of the uncertainty, it provides a more straightforward estimation.

For a more precise assessment of the uncertainty, the correlations between the probabilities could be explored by manually varying one probability and observing the corresponding changes in the others. However, in the context of this work, the assumption of uncorrelated parameters is considered sufficient.

Therefore, the uncertainty of $p_{\text{target-in, corr}}$ is calculated using Gaussian error propagation:

$$\Delta p_{\text{target-in, corr}} = \sqrt{\Delta p^2_{\text{target-in}} + \Delta p^2_{\text{InelasTO}} + \Delta p^2_{\text{ElasOut}} + (\Delta m \cdot p_{\text{InelasTM}})^2} \tag{5.24}$$

And the final corrected reaction cross-section is calculated using the corrected number of outgoing tracks and again considering the background correction from the previous section:

$$\sigma_{\text{R,corr}} = \frac{1}{n_{\text{A}}} \left[\left(\frac{N_{\text{out}}}{N_{\text{in}}} \right)_{\text{target-out}} - \left(\frac{N_{\text{out,corr}}}{N_{\text{in}}} \right)_{\text{target-in}} \right] . \tag{5.25}$$

The total uncertainty on the cross-section is derived by:

$$\Delta \sigma_{\text{R,corr}} = \frac{1}{n_{\text{A}}} \sqrt{\Delta p^2_{\text{target-out}} + \Delta p^2_{\text{target-in,corr}}} \tag{5.26}$$

5.7.3 Estimation of reaction energy

To use the cross-section for applications, it is essential to not only know the reaction cross-section but also the energy at which it is measured accurately. Therefore, a critical discussion of the uncertainty in reaction energy is crucial.

The energy uncertainty is influenced by three main factors. Firstly, there is uncertainty in the beam energy. Secondly, the uncertainty arises from the statistical nature of energy loss through the measurement setup. Lastly, the uncertainty is affected by the reaction position within the target. Since the reaction can occur at different points along the target, the particle will have varying energy at the interaction position.

Before estimating the actual uncertainty of the reaction energy, the best guess for this energy is determined. The expected measured energy E_{reac} is defined as

$$E_{\text{reac}} = E_{\text{beam}} - E_{\text{loss}}, \tag{5.27}$$

where E_{loss} defines the energy that is lost from the beam production up until the beginning of the target. This energy loss is calculated using the Catima code library [39].

The uncertainty of the reaction energy is determined by considering the dispersion of the beam energy ΔE_{beam} and the energy straggling through the measurement setup ΔE_{loss}. In addition, the energy loss in the target E_{t}, as well as its uncertainty ΔE_{t}, are taken into account for the lower limit of the reaction energy, to account for the uncertainty of the reaction position within the target.

While the beam energy is considered constant in the simulation, it is necessary to estimate the energy uncertainty for a real measurement scenario. In order to account for this, the energy dispersion of a similar medical facility, $\Delta E/E < 0.7\ \%$ [34], is assumed as an uncertainty for the beam energy. The uncertainty of E_{loss} is directly given by Catima and marks the energy straggling thought the setup up until the front of the target. To estimate the uncertainty arising from the target extension, the energy loss in the target is calculated using Catima. This calculation also gives directly the uncertainty on this loss from energy straggling.

A precise estimation of the uncertainty in the reaction cross-section is challenging due to the expected correlations among the different components. The energy loss in the setup E_{loss} is correlated with the beam energy E_{beam}. Similarly, the energy loss in the target (E_{t}) is also correlated with the beam energy and the energy loss in the setup. However, since the specific correlation behaviour is unknown, it is assumed that these variables are uncorrelated. This assumption leads to an overestimation of the uncertainty, but it is deemed acceptable in this case. Therefore, the uncertainties in the reaction cross-section are determined by:

$$\Delta E^{+}_{\text{reac}} = \sqrt{\Delta E^2_{\text{beam}} + \Delta E^2_{\text{loss}}} \qquad \Delta E^{-}_{\text{reac}} = \sqrt{\Delta E^2_{\text{beam}} + \Delta E^2_{\text{loss}} + E^2_{\text{t}} + \Delta E^2_{\text{t}}} \tag{5.28}$$

5.7.4 Results

The results of the virtual measurement are depicted in figure 5.13. The initially measured cross-section exhibits significant deviations from the expected reaction cross-section. This discrepancy is anticipated, considering the various factors contributing to track loss.

The correction for background events has a minimal impact on the cross-section due to the substantial reduction in background events achieved by limiting the accepted area for incoming tracks. For a comparison consider appendix A. The primary correction is required for false positive and false negative events, as expected from figure 5.12. The figure shows that at low proton energies, a significant number of particles scatter elastically, resulting in a lack of outgoing tracks. This effect reduces with increasing energy, which is reflected in the estimated reaction cross-section. For higher energies, the background-corrected cross-section closely aligns with the expected values. This trend is evident in figure 5.10 (right plot), where the number of false positive events decreases with energy. As expected from figure 5.12, the cross-section is overestimated at low energies, primarily due to elastic scattering, while at higher energies, it is underestimated, as the number of `ElasOut` events falls below the number of `InelasTO` events.

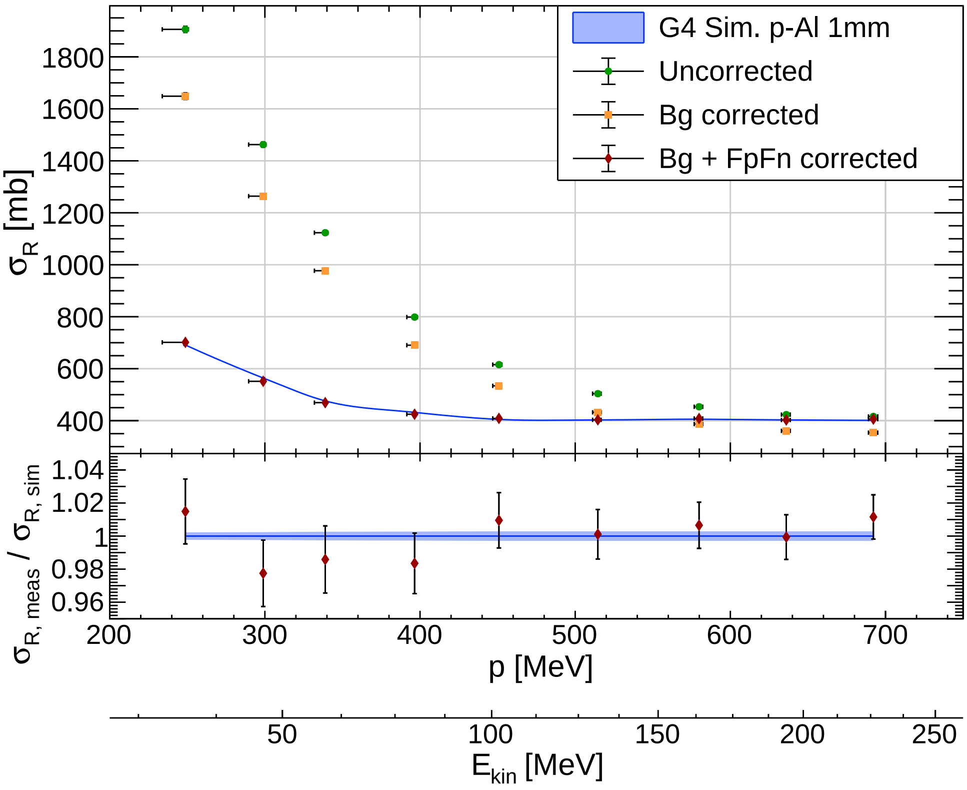

Figure 5.13: Results of the virtual reaction cross-section experiment after each analysis step: The green values represent the cross-section calculated from the raw data. The orange data points show the background-corrected (Bg) cross-section. The red points resemble the final result after correcting for background, false positive and false negative (FpFn) events.

After correcting for the number of false positive and false negative events, the measured cross-section is found to be in good agreement with the expected cross-section. The deviation between the two values is below 1σ for all measured energies. The achieved statistical uncertainty ranges from 1.9 % for the lowest energy to 1.3 % for the highest energy considered. The higher uncertainty at lower energies is attributed to a significant increase in false events that require correction. The uncertainty in the reaction energy ranges from 12 % to slightly above 0.7 %. It can be observed that for low energies, the lower limit of the reaction energy uncertainty is significantly larger than the upper limit. This is due to the larger energy loss in the target experienced at lower energies, resulting in a larger uncertainty in the reaction energy. However, as the energy increases, the energy loss in the target decreases, leading to a smaller imbalance between the lower and upper limits of the uncertainty.

It would be interesting to investigate the behaviour of uncertainties on the cross-section and energy for a thinner target. At first glance, the energy uncertainty might decrease due to reduced energy loss. However, the increased straggling could potentially worsen the overall energy uncertainty. Additionally, a thinner target would result in a decrease in the number of false positive reaction events, but the ratio of reaction events to these false positive events would also decrease significantly. Consequently, it is expected that a thinner target would lead to a higher overall uncertainty of the cross-section.

This virtual measurement serves as a confirmation that the classification used functions as intended, allowing for the reconstruction of the initially contaminated cross-section. It demonstrates the effectiveness of the correction procedure in mitigating the effects of false positive and false negative events, resulting in a cross-section that closely aligns with the expected values.

6. Summary, discussion and outlook

Summary

Measuring the reaction cross-section at relatively low energies is a pursuit that seeks the extraordinary. Typically, when a charged particle with low energy traverses a material, it undergoes energy loss and experiences a slight deviation from its original path. Occasionally, the particle scatters significantly within the material, deviating greatly from its initial trajectory. In rare cases, the particle engages in inelastic interactions, giving rise to a multitude of neutral and charged particles emitted in all directions. Although these events are infrequent, they have a significant influence in various fields of modern science and applications.

The goal of this thesis was to provide a simulation to study the feasibility of measuring the reaction cross-section of protons in an aluminium target using ALPIDE CMOS MAPS. This study aimed at finding sources of uncertainties and possibilities to mitigate them in order to help in the planning of such a measurement with the available resources. In the case of the well-known proton, there are available models that facilitate the study of the feasibility of correcting raw data using simulation models.

In the beginning, the proposed measurement technique and setup were presented. The attenuation method involves measuring the attenuation of a particle beam through a target to derive the reaction cross-section. For tracking incoming particles, three planes of ALPIDE sensors were chosen to ensure sufficient registration of incoming protons. Downstream from the target, an additional three ALPIDE sensors were placed to cover the crucial central region and provide reliability to the measurements. To enhance the measurement acceptance, two Outer Barrel Modules (OBM) were added behind the single sensors. Additionally, an upstream scintillator was positioned to trigger on incoming beam particles. The positioning of the individual components was assumed based on knowledge from previous measurements.

The measurement setup considered was reconstructed in simulation by modeling the individual components with Geant4 volumes. A sensitivity for these volumes was implemented not only to detect the protons in the detectors but also to study the interactions inside the target. To validate the model used to describe the inelastic interactions, the reaction cross-section predicted by the simulation was compared to the measurements available from earlier experiments. This comparison showed a good correspondence between simulation and measurements.

At the core of this work lies the thorough examination of the various origins of each measurement signature. This analysis has shed light on the significant impact of elastic scattering, which contributes to false positive events in the measurement. Additionally, it has revealed the presence of a substantial number of background events when no region of interest is defined to restrict the incoming tracks. These findings emphasise the importance of using appropriate corrections in order to obtain accurate and reliable results.

The study on the impact of the target thickness yielded three significant findings. Firstly, the target thickness affects the reaction rate and consequently determines the required measurement duration in order to gather sufficient statistics. Secondly, it influences the occurrence of false positive events. The ratio of true to false reaction events increases with increasing target thickness. Additionally, measurements at low energies are impractical for thick targets due to increased ionisation energy loss and proton absorption. Thirdly, the target thickness affects the uncertainty associated with the reaction energy, thereby limiting its precision.

The restriction to a region of interest for incoming tracks was considered to substantially reduce edge-related effects. Quantifying the contribution of multiple scattering from the target is particularly challenging, especially for particles located at the edge of the telescope. Scintillator-induced proton scattering results in divergent incoming tracks and potential background events. These factors served as the primary motivation for implementing the track restriction. By imposing this acceptance restriction, the number of background events decreased by one order of magnitude, enabling successful quantification of the multiple scattering contributions from the target.

The implementation of a virtual measurement was simulated to validate the classification method and verify the understanding acquired throughout this thesis. Following the background event correction using a target-out measurement, the insights gained from the simulation were applied to correct all false positive and false negative events. This correction successfully reconstructed the expected reaction cross-section.

Discussion

To provide a more comprehensive evaluation of this work, a critical discussion is conducted in two parts. Firstly, the setup and resulting effects are examined, highlighting the key aspects and their implications. Secondly, the methodology employed in this thesis is discussed, including the classification method and the correction techniques utilised.

Setup The arrival of beam particles must be signaled to trigger the recording of events.

The scintillator used for this scope has presented challenges throughout this thesis. Its thickness of 1 cm introduces a significant amount of unnecessary material into the particle beam, which has a negative impact on the measurement. While the detector must interact with the particle to measure it, it is important to minimise its influence on the particle kinematics.

The thickness of the scintillator encourages elastic scattering, resulting in divergent trajectories. These divergent trajectories contribute to the background signal if left untreated. Although the acceptance restriction on incoming tracks can help excluding these events, it increases the statistical uncertainty. Furthermore, the divergence of trajectories complicates the quantification of the multiple scattering contributions from the target.

The thickness of the scintillator also increases the likelihood of inelastic interactions occurring within the scintillator itself, leading to the possible measurement of unknown particles that contaminate the results.

Lastly, the high energy loss in the scintillator, which can be up to 30 % of the beam energy, contributes significantly to the overall uncertainty in the reaction energy.

These considerations suggest that reducing the material thickness of the trigger device is beneficial for improving the overall uncertainty of the measurement. Consequently, it is worth exploring alternative detector types to be used for triggering. The high-rate capability of the measurement setup is determined by its slowest component, namely the ALPIDE. It exhibits a peaking time of the output signal at the front-end of approximately 2 µs due to diffusion processes [2]. Therefore, possible candidates need to surpass this time while reducing the material budget compared to the scintillator.

Two intriguing designs from the range of silicon detectors should be mentioned. The first design is the emerging Low Gain Avalanche Diode (LGAD) technology, which offers high precision timing below 100 ps while maintaining a thinness of approximately 200 µm[31]. The second design worth mentioning is the TelePix sensor, which is fabricated using a 180 nm HV-CMOS process and offers a fast region of interest trigger capability, with a timing resolution on the order of a few nanoseconds and a thickness of 100 µm [9]. Both of these sensors are excellent choices as they significantly reduce the amount of material in the beam while preserving the rate capability. The TelePix sensor is particularly interesting, as its region of interest triggering capability enables the trigger area to effectively match the ALPIDE area, reducing the amount of empty events.

The second aspect under discussion is the proton beam itself. The large Full Width at Half Maximum (FWHM) of 1 cm worsens the issues mentioned for the scintillator. The proton beam trajectories are not only divergent but also spatially distributed, causing some of them to only barely hit the edges of the detectors. This results in a significant number of background events.

Although these events can be mitigated through the use of restrictions, it comes at the cost of statistics. If possible, one potential solution is to move the setup closer to the beam exit, which would result in a more focused beam due to less scattering in the surrounding air. This could help lighten some of the challenges associated with the proton beam and improve the overall quality of the measurement.

Method The method employed for analysing the simulated data was effective in reconstructing the expected reaction cross-section. The approach involved correcting for background events using a target-out measurement and correcting the number of outgoing tracks using the event classification of the simulation. The developed classification successfully achieved its goal of identifying the most significant causes of each measurement signature.

The corrections heavily rely on accurate modelling of the relevant interactions. Since the interactions of protons are well understood, the simulation was able to accurately predict their behaviour. However, it should be noted that this method may not be directly applicable to real measurement data involving unmeasured projectile-target combinations.

To achieve a precise reaction cross-section measurement, it is crucial to have good knowledge of the differential elastic cross-section and the production of secondary charged particles in inelastic interactions, prior to the measurement. This knowledge is essential for applying corrections and isolating the reaction events in the measurement of the reaction cross-section, regardless of the method chosen. Therefore, in order to assess the feasibility of using the simulation for data correction, it is necessary to examine the validity of simulation models for elastic scattering and the inelastic production of charged particles. However, if valid models are not available, traditional methods that directly utilise the measured cross-sections, rather than models, must be employed for the corrections.

Outlook

The use of MAPS in the measurement offers the significant advantage of precise position measurement and low mass. However, this aspect was not fully considered within the scope of this work. To further explore the potential of utilising MAPS and tracking outgoing particles, as an alternative to the traditional calorimetry-based approach for identifying inelastic interactions, full track reconstruction needs to be included in the analysis.

This approach has the potential advantage of spatially separating multiple protons in a single event, permitting a higher data acquisition rate. In principle, this should work since the total number of incoming and outgoing tracks is what matters, rather than determining which specific particle is lost. For instance, if each event contains two protons but only one outgoing track is registered, it is not crucial to identify which proton is missing. This has the potential to significantly increase the statistical precision.

Considering tracking becomes essential when analysing real measurement data, as factors such as detection efficiency and track reconstruction efficiency can also contribute to the loss of tracks, which needs to be corrected for. Further investigations in this direction may reveal that these corrections are already fully accounted for when correcting for background effects. Since these two quantities are independent of the target, they should similarly impact the target-out measurement.

The major advantage of using a calorimeter for this measurement is the direct counting of inelastic interactions, which leads to a reduction in statistical uncertainty compared to inferring the inelastic interactions from the count of incoming and outgoing tracks. However, recent developments have sparked interest in combining the advantages of both approaches. For example, the Bergen pCT collaboration has developed a prototype proton computer tomography (pCT) scanner, which utilises a high granularity digital tracking calorimeter as both a tracking and energy detector [6]. The device comprises a sampling calorimeter with 41 layers of absorber and detector and two additional tracking layers. Each detector layer in the calorimeter is equipped with 108 ALPIDE sensors. The possibility of simultaneously reconstructing a high multiplicity of incoming particle tracks has been demonstrated (pCT [6]). This concept is particularly intriguing for the reaction cross-section measurement, as it offers the potential to directly measure the inelastic interactions for multiple particles in one event.

The next steps in the planning of the measurement involve preparing and thoroughly testing the mechanical setup, as well as the data acquisition system. When assessing the concrete components available for use in the experiment, such as the number of OBM (as well as the thickness and distance of the ALPIDE sensors on it) and the type of trigger detector, concrete studies on the arrangement of the setup should be conducted to assess the optional arrangement and parameters. If the readout of the OBM is found to be reliable and fast enough, the idea of using only three OBM for the measurement downstream from the target becomes attractive, as it enhances the acceptance of the measurement. Nevertheless, comprehensive studies examining the effects of the gaps between the individual sensors should be conducted. Additionally, after deciding on the specific energies to be measured, the appropriate target thickness should be selected carefully. Once these preparations are completed, all that remains is to dive in the measurement.

The work presented in this thesis shows that measuring the reaction cross-section for protons using only MAPS is feasible. While the number of reaction events cannot be directly measured, a reasonable level of uncertainty can be achieved with sufficient statistics. It is essential to incorporate tracking to explore the limitations of this measurement approach. Overall, this study provides valuable insights into the crucial aspects and limiting factors of the proposed measurement.

A. Measurement without ROI

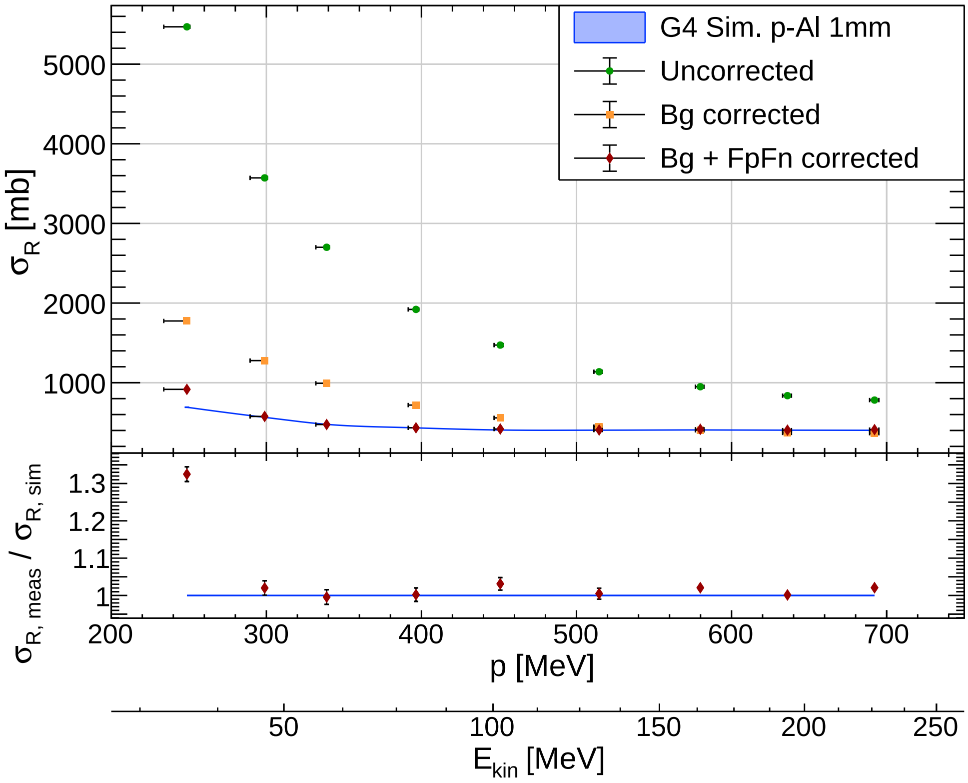

Figure A.1: Results of the virtual reaction cross-section experiment after each analysis step without using a restriction as ROI: The green values represent the cross-section calculated from the raw data. The orange data points show the background-corrected (Bg) cross-section. The red points resemble the final result after correcting for background, false positive and false negative (FpFn) events.

Without restricting the incoming tracks on a region of interes (ROI) the background shows a significantly larger contribution. For low energies the cross-section is significantly overestimated as scattering at the edge of the telescope is falsely attributed to the background and thus remains uncorrected.

Acknowledgements

I am sincerely grateful to Prof. Dr. Silvia Masciocchi for affording me the opportunity to join her team of proficient, diligent, and creative minds. Throughout this journey, her unwavering support for me has been a constant source of motivation and encouragement. I deeply appreciated her openness, empathy and invaluable experience, which have been instrumental in my personal and professional growth. Especially, I want to thank her for enabling me to participate in the thrilling test beam campaign in Krakow 2022. This experience was truly remarkable and offered me a valuable first glimpse into the world of a physicist's work. Additionally, I would like to express my gratitude to Dr. Kai Schweda for kindly accepting to be the second examiner of this thesis.

I am deeply grateful to Bogdan Blidaru, who, at all times, provided an open ear and unwavering support for me. His sense of humor always lightened the mood, fostering a friendly, warm, and inviting atmosphere. Likewise, I extend my gratitude to Pascal Becht for his valuable advice and insightful comments on my thesis.

I want to extend my heartfelt thanks to everyone who shared the office with me during long days. Their camaraderie and warmth created a familiar atmosphere. I will miss the moments we shared, especially the round of cards we rewarded ourselves with. I am truly grateful for their company and the positive spirit they brought to our work environment.

I am immensely grateful for the invaluable support I received from my beloved partner. Not only did she stand by my side and provide critical and constructive discussions to help with the work, but she also offered relentless emotional support during challenging times. Her dedication has been truly impactful and I deeply appreciate her commitment throughout this journey.

I want to express my heartfelt gratitude to my beloved and loving family. I am deeply grateful to Kurt Kalmbach for his impactful influence and guidance, which have played a vital role in shaping my character and personal growth. I am immensely proud of my mother, who made it possible for me to pursue my studies. Her unwavering support and sacrifices have been the foundation of my academic journey. Moreover, I cannot imagine a better brother who has become my greatest role models, someone I deeply look up to. His guidance, encouragement and achievements have inspired me throughout my life. I am truly fortunate to have such a remarkable family by my side.

References

[1] R.L. Workman et al. (Particle Data Group). "Review of Particle Physics". In: *Prog. Theor. Exp. Phys.* (2022).

[2] G. A. Rinella. "The ALPIDE pixel sensor chip for the upgrade of the ALICE Inner Tracking System". In: *Nucl. Instrum. Meth. A* 845 (2017). Ed. by G. Badurek et al., pp. 583–587. DOI: `10.1016/j.nima.2016.05.016`.

[3] K. Aamodt et al. "The ALICE experiment at the CERN LHC". In: *JINST* 3 (Aug. 2008), S08002. DOI: `10.1088/1748-0221/3/08/S08002`.

[4] J. Apostolakis et al. "Geometry and physics of the Geant4 toolkit for high and medium energy applications". In: *Radiation Physics and Chemistry* 78: 859-873 (2009).

[5] S. Agostinello et al. "Geant4-a simulation toolkit". In: *Nuclear Instruments and Methods in Physics Research* A 506: 250-303 (2003).

[6] J. Alme et al. "A High-Granularity Digital Tracking Calorimeter Optimized for Proton CT". In: *Frontiers in Physics* 8 (Oct. 2020), p. 460. DOI: `10.3389/fphy.2020.568243`.

[7] G. Antchev et al. "Measurement of elastic pp scattering at $\sqrt{s} = 8$ TeV in the Coulomb–nuclear interference region: determination of the ρ-parameter and the total cross-section". In: *The European Physical Journal C* 76.12 (Nov. 2016), p. 661. ISSN: 1434-6052. DOI: `10.1140/epjc/s10052-016-4399-8`. URL: `https://doi.org/10.1140/epjc/s10052-016-4399-8`.

[8] M. Asai. *Introduction To Geant4*. Available at `https://cds.cern.ch/record/491492/files/p107.pdf` (2023/06/05).

[9] H. Augustin et al. "TelePix – A fast region of interest trigger and timing layer for the EUDET Telescopes". In: *Nuclear Instruments and Methods in Physics Research Section A: Accelerators, Spectrometers, Detectors and Associated Equipment* 1048 (Mar. 2023), p. 167947. DOI: `10.1016/j.nima.2022.167947`. URL: `https://doi.org/10.1016%2Fj.nima.2022.167947`.

[10] R.F. Carlson. "Proton-Nucleus Total Reaction Cross Sections and Total Cross Sections Up to 1 GeV". In: *Atomic Data and Nuclear Data Tables* 63.1 (1996), pp. 93–116. ISSN: 0092-640X. DOI: `https://doi.org/10.1006/adnd.1996.0010`. URL: `https://www.sciencedirect.com/science/article/pii/S0092640X96900108`.

[11] R.F. Carlson et al. "A technique for measuring proton total reaction cross sections at medium energies". In: *Nuclear Instruments and Methods* 123.3 (1975), pp. 509–519. ISSN: 0029-554X. DOI: `https://doi.org/10.1016/0029-554X(75)90205-0`. URL: `https://www.sciencedirect.com/science/article/pii/0029554X75902050`.

[12] M. Casolino et al. "Space travel: Dual origin of light flashes seen in space". In: *Nature* 422 (2003), p. 680.

[13] ALICE Collaboration. "Letter of intent for ALICE 3: A next-generation heavy-ion experiment at the LHC". In: *CERN-LHCC-2022-009* 2 (2022).

[14] ALICE Collaboration. *The ALICE experiment – A journey through QCD*. 2022. arXiv: `2211.04384 [nucl-ex]`.

[15] Geant4 Collaboration. *Book For Application Developers*. 11.1. geant4, 2022.

[16] Geant4 Collaboration. *Physics Reference Manual*. 11.1. geant4, 2022.

[17] Wikimedia Commons. *Standard model of elementary particles*. Available at `https://commons.wikimedia.org/wiki/File:Standard_Model_of_Elementary_Particles.svg` (2023/14/05).

[18] M.H. Kelsey D. H. Wright. "The Geant4 Bertini Cascade". In: *Nuclear Instruments and Methods in Physics Research A* 804 (2015), pp. 175–188.

[19] I. M. Dremin. "Elastic scattering of hadrons". In: *Phys. Usp.* 56 (2013), pp. 3–28. DOI: `10.3367/UFNe.0183.201301a.0003`. arXiv: `1206.5474 [hep-ph]`.

[20] Eljen Technology. *General purpose EJ-200, EJ-204, EJ-208, EJ-212*. Available at `https://eljentechnology.com/products/plastic-scintillators/ej-200-ej-204-ej-208-ej-212` (2023/11/07).

[21] D. Franco. *G4EmStandardPhysics.cc File Reference*. Available at `https://apc.u-paris.fr/~franco/g4doxy/html/G4EmStandardPhysics_8cc.html` (2023/15/05).

[22] G. Folger, J. P. Wellisch. "The Binary Cascade". In: *The European Physical Journal A - Hadrons and Nuclei* 21 (2004), pp. 407–417.

[23] ALICE Collaboration homepage. *ALICE EMCAL*. Available at `https://alice-collaboration.web.cern.ch/menu_proj_items/emcal` (2023/31/06).

[24] ALICE Collaboration homepage. *ALICE PHOS*. Available at `https://alice-collaboration.web.cern.ch/menu_proj_items/phos-cpv` (2023/31/06).

[25] ALICE Collaboration homepage. *ALICE Tof.* Available at `https://alice-collaboration.web.cern.ch/menu_proj_items/tof` (2023/31/06).

[26] CERN hompage. *The accelerator complex.* Available at `https://www.home.cern/science/accelerators/accelerator-complex` (2023/11/05).

[27] CERN hompage. *The Large Hadron Collider.* Available at `https://home.cern/science/accelerators/large-hadron-collider` (2023/11/05).

[28] M. S. Smith K. E. Rehm. "Nuclear astronphysics measurements with radioactive beams". In: *Annu. Rev. Nucl. Part. Sci.* 51 (2001), p. 91.

[29] A. Kaiser. *Tracking low momentum protons with the ALICE Pixel Detector.* Physikalisches Institut Universität Heidelberg. Aug. 2023.

[30] H. Kolanoski and N. Wermes. *Particle Detectors: Fundamentals and Applications.* Oxford University Press, 2020. ISBN: 9780198858362.

[31] W. Krüger et al. "LGAD technology for HADES, accelerator and medical applications". In: *Nuclear Instruments and Methods in Physics Research Section A: Accelerators, Spectrometers, Detectors and Associated Equipment* 1039 (2022), p. 167046. ISSN: 0168-9002. DOI: `https://doi.org/10.1016/j.nima.2022.167046`. URL: `https://www.sciencedirect.com/science/article/pii/S0168900222004697`.

[32] M. Lantz. *Investigations of Reaction Cross Sections for Protons and 3He.* Available at `http://uu.diva-portal.org/smash/get/diva2:166486/FULLTEXT01.pdf` (2023/10/07). May 2005.

[33] F. Luoni et al. "Total nuclear reaction cross-section database for radiation protection in space and heavy-ion therapy applications". In: *New Journal of Physics* 23.10 (Oct. 2021), p. 101201. DOI: `10.1088/1367-2630/ac27e1`. URL: `https://dx.doi.org/10.1088/1367-2630/ac27e1`.

[34] A. Maj. *Nuclear Physics Research At The Medical Proton Therapy Center CCB In Krakow.* Available at `https://ispun23.vn/public/presents/Maj_ISPUN2023.pdf` (2023/28/06). May 2023.

[35] S. Masciocchi. "Physics of particle detectors - Interaction of particles with matter 1". In: *Presentation slides 25 April, Master course (summer term), University of Heidelberg* (2022).

[36] A. Papoulis and U. Pillai. "Probability, Random Variables, and Stochastic Processes, Fourth Edition". In: (Jan. 2002).

[37] Geant4 homepage PhysicsListGuide. *FTFP_BERT.* Available at `https://geant4-ed-project.pages.in2p3.fr/geant4-ed-web/docs/physics_more.pdf` (2023/27/06).

[38] Geant4 homepage PhysicsListGuide. *QBBC.* Available at `https://geant4-userdoc.web.cern.ch/UsersGuides/PhysicsListGuide/html/reference_PL/QBBC.html` (2023/15/05).

[39] A. Prochazka. "Catima Physics Manual". In: (Dec. 2020). URL: `https://www.isotopea.com/webatima/catima.pdf`.

[40] W.D. Newhauser R. Zang. "The physics of proton therapy". In: *Phys. Med. Biol.* 60 (2015).

[41] F. Reidt on behalf of the ALICE collaboration. "Upgrade of the ALICE ITS detector". In: *Nuclear Instruments and Methods in Physics Research A* 1032 (2022).

[42] J. Schuhkraft. "Heavy-ion physics with the ALICE experiment at the CERN Large Hadron Collider". In: *Phil. Trans. Roy. Soc. Kond.* 370 (2012), pp. 917–932.

[43] K. Skjerdal. "Photoproduction of ρ^0 in ultra-peripheral nuclear collisions at ALICE". In: *J.Phys.:Conf.Ser.* 455 (2013).

[44] A. J. Koning A. Hasegawa T. Fukahori. "Intermediate Energy Data". In: *NEA REPORT NEA/WPEC* 13 (1998).

[45] M. Thomson. *Modern Particle Physics.* Cambridge University Press, 2013.

[46] Tower Partners Semiconductor Co., Ltd. *Official website of Tower semiconductor.* Available at `https://towersemi.com` (2023/17/07).

[47] J.H. Trainor. "Instrument and spacecraft faults associated with nuclear radiation in space". In: *Advances in Space Research* 14 (1994), p. 685.

[48] M. Verderi. *Physics Content Of GEANT4.* Available at `https://geant4-userdoc.web.cern.ch/UsersGuides/PhysicsListGuide/html/reference_PL/QBBC.html` (2023/15/05). May 2023.

[49] A. Ribon W. Pokorski. *Detector Simulation.* Available at `https://indico.cern.ch/event/294651/sessions/55918/attachments/552022/760636/detector_simulation_lecture_ribon_esipap2014.pdf` (2023/06/05).

[50] R. L. Workman et al. "Review of Particle Physics". In: *PTEP* 2022 (2022), p. 083C01. DOI: `10.1093/ptep/ptac097`.

Declaration

I declare that this thesis has been composed solely by myself. Except where states otherwise by references or acknowledgment, the work presented is entirely my own.

Erklärung

Ich versichere, dass ich diese Arbeit selbstständig verfasst und keine anderen als die angegebenen Quellen und Hilfsmittel benutzt habe.

Heidelberg, den 04.08.2023